
A MONOSEMANTIC ATTRIBUTION FRAMEWORK FOR STABLE INTERPRETABILITY IN CLINICAL NEUROSCIENCE LARGE LANGUAGE MODELS

Michail Mamalakis

Department of Computer Science and Technology
Cancer Research UK Cambridge Institute
University of Cambridge
United Kingdom
mm2703@cam.ac.uk

Tiago Azevedo

Department of Computer Science and Technology
University of Cambridge
United Kingdom

Cristian Cosentino

DIMES
University of Calabria
Italy

Chiara D'Ercoli

Department of Computer
Automatic and Management Engineering (DIAG)
Sapienza Università di Roma
Italy

Subati Abulikemu

Department of Psychiatry
University of Cambridge
United Kingdom

Zhongtian Sun

School of Computing
University of Kent
United Kingdom

Richard Bethlehem

Department of Psychology
University of Cambridge
United Kingdom

Pietro Lio

Department of Computer Science and Technology
University of Cambridge
United Kingdom

January 27, 2026

ABSTRACT

Interpretability remains a key challenge for deploying large language models (LLMs) in clinical settings such as Alzheimer's disease progression diagnosis, where early and trustworthy predictions are essential. Existing attribution methods exhibit high inter-method variability and unstable explanations due to the polysemantic nature of LLM representations, while mechanistic interpretability approaches lack direct alignment with model inputs and outputs and do not provide explicit importance scores. We introduce a unified interpretability framework that integrates attributional and mechanistic perspectives through monosemantic feature extraction. By constructing a monosemantic embedding space at the level of an LLM layer and optimizing the framework to explicitly reduce inter-method variability, our approach produces stable input-level importance scores and highlights salient features via a decompressed representation of the layer of interest, advancing the safe and trustworthy application of LLMs in cognitive health and neurodegenerative disease.

Keywords Mechanistic Interpretability · explainable AI · Attributional Interpretability · Alzheimer · monosemantic · polysemantic

1 Introduction

Explainable Artificial Intelligence (XAI) plays a crucial role in building trust in machine learning systems, especially in sensitive and high-stakes areas such as finance, climate, and healthcare [1, 2]. In medical settings, interpretability is essential for clinical integration and regulatory approval, especially in complex diseases such as Alzheimer's Disease (AD) progression [3], where early and accurate detection can substantially alter treatment results [4].

Although machine learning has shown promise in Alzheimer’s progression (AD) diagnostics using multimodal clinical data [5], the application of large language models (LLMs) such as GPT-4 and LLaMA-2 in structured clinical settings remains limited [6, 7]. A key obstacle is the *polysemanticity* of internal neural representations—individual neurons or features often encode multiple, semantically unrelated concepts [8, 9, 10]. This entanglement undermines the interpretability of standard attribution techniques such as gradients, perturbations, and integrated paths, which typically assume one-to-one correspondence between features and meanings. To this end, existing attribution methods assign importance scores to input features (e.g., words or tokens), yet they fall short in addressing the polysemantic nature of internal representations. This limitation often leads to ambiguous or misleading explanations—particularly problematic in clinical applications, where interpretability is critical [11, 12, 13, 14]. Moreover, the inter-method variability of attributional techniques is another limitation of dataset-driven explanations, as it reduces trust in the interpretability of AI models [15].

In contrast, mechanistic interpretability aims to uncover the internal structure of neural computation by identifying semantically coherent components within the model. Sparse Autoencoders (SAE) have played a pivotal role in advancing our understanding of such representations in both language and vision domains [16]. SAEs aim to solve the superposition problem in neural feature representations by mapping the model’s activations into a more monosemantic latent space, where individual features are better aligned with specific concepts in the network [9]. However, these mechanistic tools typically lack attributional resolution, limiting their utility for explaining how specific inputs contribute to model predictions in real-world, decision-critical scenarios [10].

This reveals a critical gap in the current landscape: attributional techniques offer only surface-level explanations using polysemantic features, while mechanistic methods provide structural insights based on monosemantic feature alignment but lack attributional grounding. To date, no unified framework successfully integrates both paradigms—particularly in the domain of LLM-based clinical inference.

To address these challenges and produce stable, clinically meaningful explanations from large language models, we propose a unified monosemantic attribution framework that integrates both attributional and mechanistic interpretability approaches (Figure 1). Our approach first employs sparse autoencoders (SAEs) to transform polysemantic LLM activations into a more monosemantic latent space, where individual features are encouraged to correspond to disentangled semantic factors. This bottleneck substantially reduces representational complexity and enables classical attribution methods to assign more precise and semantically coherent importance scores. For the attribution component, we apply six established techniques—Feature Ablation, Layer Activations, Layer Conductance, Layer Gradient SHAP [17], Layer Integrated Gradients [18], and Layer Gradient \times Activation—both in the native activation space (polysemantic features) and in the SAE-induced latent space (more monosemantic features).

To address the inter-method variability problem [15], we combine the resulting attribution vectors and introduce the *Transformer Explanation Optimizer* (TEO), a learning-based optimization mechanism that selects explanations with maximal alignment to model behavior and dataset-level consistency [15]. We experiment with encoder-decoder architectures based on 1D transformers (TEO) and diffusion networks (DEO). For meta-level assessment and visualization, we embed these optimized attributions into a 2D manifold using UMAP [19] and principal component analysis (PCA) [20], and impose a global coherence constraint by evaluating their linear structure along the primary UMAP components. This geometry-aware constraint acts as an additional regularizer, imposing a global linear structure along the dominant statistical directions of the explanation space (the first two principal components from PCA). By doing so, the principal global feature patterns exhibit similar behavior across the majority of the cohort, facilitating the extraction of robust, population-level patterns.

2 Hypothesis and Evaluation Protocol

The central hypothesis of this work is that *as the embedding layer approaches a more monosemantic representation, attribution scores become more stable, less complex, and more diagnostically informative compared to those derived from polysemantic features*. This hypothesis is evaluated through a series of experiments in which different LLMs are trained and evaluated on ADNI [21] (Independent and Identically Distributed; **IID**) and subsequently tested on BrainLAT [22] (Out-of-Distribution; **OOD**) to assess robustness under demographic and protocol shifts. We study both **binary classification** (Control vs. Alzheimer’s disease (AD)) and **three-class classification** settings (Control, Early Mild Cognitive Impairment (EMCI), and Late Mild Cognitive Impairment (LMCI) in ADNI; Control, Frontotemporal Dementia (FTD), and AD in BrainLAT).

The data are partitioned into 80% training and 20% validation within the training portion (which itself constitutes 80% of the full dataset), with the remaining 20% held out for testing. The last-layer embeddings of the LLM achieving the strongest baseline performance are subsequently used to evaluate the proposed interpretability framework.

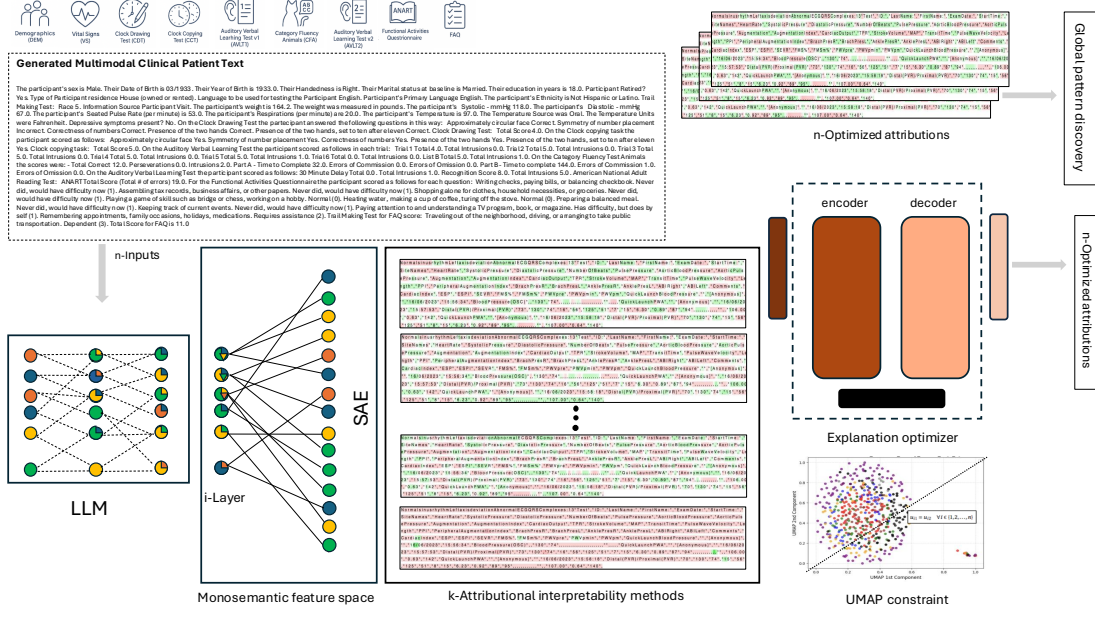


Figure 1: Proposed interpretability framework for LLM in Alzheimer’s diagnosis. The model integrates k-attributional methods with a SAE to generate a monosemantic feature space. An explanation optimizer refines attribution outputs, enhancing clarity and reducing variability. Global explanation quality is visualized and assessed using UMAP and a linear meta-rule, supporting both individual prediction interpretability and cohort-level pattern discovery.

Importantly, both the SAE bottleneck architectures (TopK, JumpReLU, and Gated-SAEs) and TEO (with and without the SAE bottleneck) are trained exclusively on IID explanation cohorts using only these training and validation splits and are then evaluated on the **OOD** dataset **without any additional training or adjustments**, enabling a rigorous assessment of out-of-distribution robustness under strict generalization conditions.

3 A Monosemantic Attribution Framework

3.1 Attributional Theory and Methods

Attribution explainability methods follow the framework of additive feature attribution, where the explanation model $g(f, \mathbf{x})$ is represented as a linear function of simplified input features:

$$g(f, \mathbf{x}) = \phi_0 + \sum_{i=1}^M \phi_i x_i \quad (1)$$

Here, f is the predictive model, $\phi_i \in \mathbb{R}$ is the attribution (importance) assigned to feature x_i , and M is the number of simplified input features (here 512).

For this study, we employed six well-established attributional interpretability methods applied to large language models (LLMs), denoted as $K = 6$: *Feature Ablation*, *Layer Activations* (which capture the embedding activation space of a specific layer of interest within the LLM), *Layer Conduction*, *Layer Gradient-SHAP* [23], *Layer Integrated Gradients* [18], and *Layer Gradient \times Activation* (For analytical mathematic formulation see Appendix A.1.). To align these layer-wise interpretability methods with the additive feature attribution framework, we reinterpret the internal activations (i.e., latent units) of a network layer L as simplified input features. The objective is to estimate an attribution score ϕ_i for each unit, where $\phi_i \in \mathbb{R}$ quantifies the contribution of the corresponding neuron to the model’s prediction.

All attribution methods were applied to the final (22nd) layer of the MODERN-BERT LLM—the model variant that achieved the highest classification accuracy in our evaluations (see Supplementary section 1.2). These formulations allow us to ground various neural attribution techniques within a unified additive explanation model, facilitating their comparison and hybridization under shared theoretical assumptions.

3.2 Attributational Explanation Optimizer Framework

Let $\mathcal{A} = \{A_1, A_2, \dots, A_K\}$ denote the set of $K = 6$ attribution methods applied to the final layer L of the model f . Each method A_k generates an attribution vector $\phi^{(k)} = [\phi_1^{(k)}, \phi_2^{(k)}, \dots, \phi_M^{(k)}]$, where M is the number of latent features (neurons) in layer L . The goal is to derive a unified attribution vector $\bar{\phi}$ that captures the consensus explanation across methods. Each attribution vector $\phi^{(k)}$ is evaluated using the Relative Input Stability (RIS), Relative Output Stability (ROS) [24], and Sparseness [25] metrics (Appendix A.2.). The weighted average attribution vector $\bar{\phi}$ serves as the target explanation for the optimization process and it is calculated as:

$$\bar{\phi} = \sum_{k=1}^K w_k \cdot \phi^{(k)} \quad (2)$$

An encoder-decoder model is trained to generate a reconstructed explanation $\hat{\phi}$ from the original input x . Two architectures are considered the Diffusion UNet1D [26] (*Diffusion Explanation Optimizer*, DEO) and the x-transformer autoencoder [27, 28] (*Transformer Explanation Optimizer*, TEO). For the analytical mathematical formulation, see Appendix A.2.4. As previously highlighted, the reconstruction of the optimal explanation and the associated cost function adhere to the same principles and architectural design outlined in [15]. The cost function consists of three key components: sparseness, as defined in [25]; ROS and RIS scores [24]; and similarity. The integration of these components ensures a robust and interpretable evaluation. The total cost function for training the reconstruction model is:

$$\begin{aligned} \mathcal{L}_{\text{total}}(\phi^{(k)}, \hat{\phi}) = & \lambda_1 \cdot \frac{1}{M_{\text{RIS}}(f, \hat{\phi})} + \lambda_2 \cdot \frac{1}{M_{\text{ROS}}(f, \hat{\phi})} \\ & + \lambda_3 \cdot M_{\text{sparse}}(f, \hat{\phi}) + \lambda_4 \cdot \mathcal{L}_{\text{similarity}}(\hat{\phi}, \bar{\phi}) \end{aligned} \quad (3)$$

where: $\lambda_1, \lambda_2, \lambda_3, \lambda_4$ are hyperparameters controlling the influence of each loss term. This formulation enables a principled and quantitative integration of multiple attribution methods, optimizing toward a robust and interpretable explanation.

3.3 UMAP Linear Constraint

To obtain a unified and comparable low-dimensional representation of attribution scores across all tokenizer features, we apply a feature-wise UMAP projection to the normalized attribution tensor of shape $\mathbb{R}^{M \times T}$, where M is the number of test samples and T denotes the dimensionality of the tokenizer embedding space. For each feature j , the attribution vector $x^{(j)} \in \mathbb{R}^M$ is min–max normalized and embedded using a one-dimensional UMAP transformation into a two-dimensional space $y^{(j)} \in \mathbb{R}^{M \times 2}$. The resulting coordinates are normalized to $[0, 1]$ so that all feature-wise embeddings share a common bounded range. This nonlinear projection preserves the local neighborhood structure of each attribution distribution while mapping all T tokenizer features into an aligned and directly comparable representation space across attribution methods (Appendix A.4).

Linear Constraint on UMAP Embeddings: To encourage structural consistency in the UMAP [19] embeddings, we introduce a linear constraint requiring equality between the first and second embedding components for each point, expressed as $u_{i1} = u_{i2}$. This can be written equivalently as $u_{i1} - u_{i2} = 0$ for all i . We incorporate this constraint into the overall optimization objective via a penalty term,

$$\lambda_5 \sum_{i=1}^n (u_{i1} - u_{i2})^2,$$

where λ_5 controls the strength of the constraint. This formulation enforces consistency of the reconstructed embeddings while preserving flexibility in the learned attribution representation.

3.4 The SAE Approach and Architectures

The mathematical formulation situates SAE architectures within the theoretical framework of superposition and semantic disentanglement (for an analytical mathematical formulation, see Appendix A.5). By expressing hidden states as sparse linear combinations of interpretable features, SAEs bridge the gap between low-level activations and human-understandable concepts. Let $\mathbf{x} \in \mathbb{R}^d$ denote a layer's neuron activation vector in a pretrained model. A Sparse Autoencoder learns a sparse feature representation $\mathbf{a} \in \mathbb{R}^F$ such that:

$$\hat{\mathbf{x}} = W\mathbf{a} + \mathbf{b}, \quad (4)$$

where $W \in \mathbb{R}^{d \times F}$ is the decoder (dictionary) matrix and $\mathbf{b} \in \mathbb{R}^d$ is a learned bias term. Each column $W_{:,i}$ represents the direction of feature i in neuron space, and a_i is its activation. This linear mapping enables complex activations to be expressed as combinations of more interpretable features. If $F > d$, then the feature space is overcomplete, and W cannot be full-rank. This leads to superposition, where multiple features overlap in the same subspace, and individual neurons encode multiple unrelated concepts [29]. If W is invertible and aligned to a basis, each neuron corresponds to a single feature. The representation is monosemantic and disentangled [8]. When W has overlapping columns, neurons can respond to multiple features, yielding polysemantic behavior. That is, for some j , $x_j = \sum_i W_{j,i} a_i$ involves multiple nonzero terms [30]. Variants of SAEs like TopK, JumpReLU, and Gated-SAEs offer increasingly precise control over the mapping between low-level activations and human-understandable concepts, enabling fine-grained analysis and intervention (analytical mathematical formulation, see Appendix A.6.).

3.5 Attribution from Sparse Feature Space to Input Tokens

Let $\mathbf{x}_{\text{input}} \in \mathbb{R}^{d_{\text{input}}}$ denote the input embedding vector (e.g., LLM token embeddings), $\mathbf{x} = f(\mathbf{x}_{\text{input}}) \in \mathbb{R}^d$ the hidden layer activation of the LLM, $\mathbf{a} = \text{Encoder}(\mathbf{x}) \in \mathbb{R}^F$ the SAE sparse feature vector, and $\hat{\mathbf{x}} = W\mathbf{a} + \mathbf{b}$ the reconstructed activation from the SAE decoder. Now suppose we have a sparse attribution vector ψ_i over features \mathbf{a} , i.e., $\psi \in \mathbb{R}^F$, where each ψ_i reflects the importance of SAE feature a_i . We aim to assign importance Φ_k to each input token dimension $x_{\text{input},k}$.

We propagate the feature attributions backward through the encoder to the input. Using the chain rule:

$$\Phi_k = \sum_{i=1}^F \psi_i \cdot \frac{\partial a_i}{\partial x_{\text{input},k}} = \sum_{i=1}^F \psi_i \cdot \frac{\partial a_i}{\partial \mathbf{x}} \cdot \frac{\partial \mathbf{x}}{\partial x_{\text{input},k}} \quad (5)$$

where $\frac{\partial a_i}{\partial \mathbf{x}}$ is the encoder Jacobian (SAE layer), and $\frac{\partial \mathbf{x}}{\partial x_{\text{input},k}}$ is the LLM gradient from input token to hidden layer. This gives us a scalar attribution $\Phi_k \in \mathbb{R}$ for each token/input embedding dimension k . This represents how much each input token contributes to the sparse SAE features identified as important. In doing so, we assess the contribution of input features based on the monosemantic behavior of the trained network's internal mechanisms. Building on our study, we apply the six previously discussed attribution methods at two levels: from the SAE feature space to the encoder layer, and from the encoder layer to the input embedding space. This dual-level attribution analysis enables us to investigate how interpretable sparse features relate to model internals and ultimately shape the input-level representations. Attribution methods (e.g., Integrated Gradients, SHAP) can directly estimate:

$$\boldsymbol{\phi}^{\text{input}} = \text{AttributionMethod}(f, \mathbf{x}_{\text{input}}, \boldsymbol{\phi}^{\text{SAE}}) \quad (6)$$

where $\boldsymbol{\phi}^{\text{SAE}}$ denotes the monosemantic feature space of the SAE network. Thus, the dual-level approach allows us to connect semantically meaningful sparse features to the raw input representation space.

3.6 LLM Networks and Hyperparameter Tuning

We evaluate encoder-based LLMs (BERT, RoBERTa, DistilBERT, ALBERT, BioBERT, ModernBERT) on ADNI (IID) and BRAINLAT (OOD) under a unified protocol spanning full fine-tuning, zero-shot, few-shot with temperature control, and parameter-efficient LoRA. *ModernBERT* outperformed all other networks on ADNI: in the binary task it achieved the highest F1 (75.89%), AUC-PR (86.41%), ROC-AUC (83.95%), and Accuracy (72.37%), and it remained strongest in the three-class setting (F1 68.80%, AUC-PR 78.48%, ROC-AUC 78.67%, Accuracy 65.05%). For OOD model adaptation, *ModernBERT* zero-shot yielded 55% Accuracy, few-shot/LoRA provided modest gains (62%), while full fine-tuning peaked at ~84% Accuracy but lies outside our scope (Supplementary 1.2). Accordingly, we use *ModernBERT* fine-tuned on ADNI for IID and zero-shot on BRAINLAT for OOD, and all interpretability analyses are conducted on the 22nd layer of *ModernBERT*. We conducted extensive hyperparameter tuning for all components. The explanation optimizer performed best at a learning rate of $2e^{-4}$, with the optimal weight configuration $(\lambda_1, \lambda_2, \lambda_3, \lambda_4) = (0.1, 0.3, 0.1, 0.5)$. UMAP constraints were most effective at the 4 \times batch size level (4 \times 64) (Supplementary 1.3; Figures 3). Among the four SAE variants, TopK produced the strongest overall performance (Supplementary 1.3; Figures 2, 4, 5), using a 32 \times feature depth. All models were trained using the AdamW optimizer with early stopping and standard evaluation metrics (Supplementary 1.3).

3.7 Dataset and Code Availability

The dataset used in this study originates from the ADNI cohort [21] and is represented as text generated from multiple modalities, serving as the in-distribution (IID) dataset. We further split the generated text into nine

Table 1: Unified attribution performance across tasks and evaluation settings. Values report mean \pm std per class. Binary tasks use (A/C); three-class tasks use (L/M/C) and (A/F/C). Bold indicates the best performance within each setting.

Task & Setting	Method (variant)	Sparseness	RIS	ROS
Binary — IID (ADNI) Columns: (A/C)				
Gradient Activation	0.3277 \pm 0.0384/0.2500 \pm 0.0230	5.6149 \pm 0.0193/5.6170 \pm 0.0221	16.9303 \pm 0.0034/16.9347 \pm 0.0	
Gradient Activation-SAE	0.2035 \pm 0.0117/0.1668 \pm 0.0072	5.6252 \pm 0.0213/5.6173 \pm 0.0221	16.9343 \pm 6.8e -5 /16.9347 \pm 4.0e -5	
DEO	0.3383 \pm 0.0033/0.3377 \pm 0.0017	9.2839 \pm 0.0800/9.3131 \pm 0.1427	20.6342 \pm 0.0866/20.6150 \pm 0.2026	
DEO-SAE	0.3374 \pm 0.0029/0.3140 \pm 0.0010	9.2790 \pm 0.0646/9.1750 \pm 0.1088	20.6150 \pm 0.0880/20.5150 \pm 0.1299	
TEO	0.4220 \pm 0.0003/0.4199 \pm 0.0005	5.0520 \pm 0.0192/5.0688 \pm 0.0184	16.3529 \pm 0.0056/16.3777 \pm 0.0011	
TEO-SAE	0.2672 \pm 0.0010/0.2682 \pm 0.0007	1.6227 \pm 0.1708/0.9964 \pm 0.2639	12.9250 \pm 0.1703/12.2983 \pm 0.2613	
TEO-UMAP (SAE)	0.3989 \pm 0.0004/0.4057 \pm 0.0003	5.4394 \pm 0.0332/5.4709 \pm 0.1746	16.3037 \pm 0.0033/16.2102 \pm 0.0079	
Binary — OOD (BrainLAT) Columns: (A/C)				
Gradient Activation-SAE	0.1140 \pm 0.0177/0.0630 \pm 0.0069	6.0328 \pm 0.0277/6.0339 \pm 0.0398	16.9347 \pm 3.6e -6 /16.9348 \pm 3.7e -5	
TEO-SAE	0.2691 \pm 0.0016/0.2725 \pm 0.0004	0.6835 \pm 0.6676/0.4734 \pm 0.2801	11.5236 \pm 0.6591/11.2130 \pm 0.5150	
TEO-UMAP (SAE)	0.3989 \pm 0.0005/0.4043 \pm 0.0029	5.4394 \pm 0.0383/5.4282 \pm 0.1944	16.3037 \pm 0.0039/16.1577 \pm 0.1054	
Three-class — IID (ADNI) Columns: (L/M/C)				
Gradient Activation	0.3839 \pm 0.0177/0.2917 \pm 0.0200/0.2697 \pm 0.0061	5.6272 \pm 0.0212/5.6269 \pm 0.0193/5.6290 \pm 0.0225	16.9339 \pm 0.0008/16.9340 \pm 0.0006/16.9347 \pm 0	
Gradient Activation-SAE	0.4310 \pm 0.1156/0.2579 \pm 0.1095/0.2296 \pm 0.0036	5.6297 \pm 0.9478/5.6172 \pm 1.1684/5.6210 \pm 0.0194	16.9347 \pm 2.8625/16.9347 \pm 3.5241/16.9348 \pm 1.22e -5	
TEO	0.4131 \pm 0.0003/0.3909 \pm 0.0047/0.3918 \pm 0.0008	5.0938 \pm 0.0188/4.8283 \pm 0.0377/4.8080 \pm 0.0184	16.4043 \pm 0.0024/16.1354 \pm 0.0324/16.1172 \pm 0.0090	
TEO-SAE	0.2860 \pm 0.0374/0.2838 \pm 0.0523/0.2682 \pm 0.0649	2.2642 \pm 0.4877/2.1617 \pm 0.4547/1.5468 \pm 0.1171	13.5646 \pm 2.2745/13.4676 \pm 2.7641/12.8570 \pm 0.1179	
TEO-UMAP (SAE)	0.4161 \pm 0.0870/0.4172 \pm 0.2372/0.3973 \pm 0.0749	5.1017 \pm 0.1697/5.1116 \pm 0.1072/5.1086 \pm 0.2083	16.4031 \pm 3.8616/16.4088 \pm 0.4924/16.4123 \pm 6.8439	
Three-class — OOD (BrainLAT) Columns: (A/F/C)				
Gradient Activation-SAE	0.1836 \pm 0.0016/0.4303 \pm 0.0022/0.1772 \pm 0.0112	6.0269 \pm 0.0302/6.1450 \pm 0.1210/6.1234 \pm 0.1912	16.9348 \pm 2.6e -6 /16.9345 \pm 2.8e -5 /16.9346 \pm 1.5e -5	
TEO-SAE	0.3716 \pm 0.0009/0.4224 \pm 0.0002/0.4162 \pm 0.0029	4.9396 \pm 0.0148/5.5421 \pm 0.0611/5.7520 \pm 0.3645	15.8121 \pm 0.0099/16.2773 \pm 0.0010/16.3792 \pm 0.0034	
TEO-UMAP (SAE)	0.4239 \pm 5.0e -4 /0.4246 \pm 2.4e -4 /0.4238 \pm 5.6e -4	5.4583 \pm 0.0297/5.5576 \pm 0.0954/5.5525 \pm 0.1862	16.3726 \pm 0.0017/16.3572 \pm 0.0035/16.3661 \pm 0.0073	

subgroups based on input modality, as detailed in Supplementary Material 1.1.5, for pattern analysis and biomarker research purposes. For the out-of-distribution (OOD) cohort, we used text generated from multimodal sources (MRI and clinical files) in the Latin American Brain Health Institute (BrainLat) dataset, a multi-site initiative providing neuroimaging, cognitive, and clinical data across several Latin American countries [22]. Additional demographic and preprocessing details are provided in Supplementary Sections 1.1.1–1.1.5. The code is implemented in Python using PyTorch and runs on an NVIDIA cluster in one A100-SXM-80GB GPU. It leverages SAE_LENs [31] for SAE training, quantus [32] for evaluation, and captum for attribution analysis.

4 Results of Experiments

4.1 Ablation Analysis of the Monosemantic Attribution Framework

In this study, sparseness is defined such that higher values correspond to more selective and concentrated attributions across input features—that is, greater sparseness. However, sparseness alone is insufficient to assess explanation quality, as it does not account for robustness or stability. Therefore, the most effective explanation method is one that simultaneously achieves high sparseness and low RIS and ROS values.

Across IID, OOD datasets and for both binary and three-class classification tasks, Table 1 shows a consistent stability-sparsity frontier governed by the proposed optimizers. In the binary IID case, SAE substantially improves stability for feature-learning explainers, most notably: Layer Conductance and especially TEO, with large drops in RIS/ROS for both Alzheimer’s and Control, whereas Activation-SAE increases RIS/ROS relative to its no-SAE variant and is therefore less robust. In the binary OOD case, this pattern persists and strengthens: TEO-SAE achieves the lowest RIS/ROS overall (strong cross-dataset stability), while TEO-UMAP recovers higher sparsity (> 0.40) at a modest stability cost versus TEO-SAE, offering a tunable sparsity–stability trade-off. In the three-class IID setting, Feature Ablation is the sparsity leader across Control/LMCI/MCI (~ 0.52 – 0.53) with moderate, steady yet still high RIS/ROS values; Layer Conductance-SAE markedly reduces RIS/ROS for LMCI/MCI; and TEO-SAE again delivers the most stable attributions across all classes, albeit with reduced sparsity compared with no-SAE variants. The same rank ordering holds OOD. Across all blocks, gradient-formulaic methods (Grad-SHAP, Guided Backprop, Integrated Gradients) show near-invariant RIS/ROS (~ 5.6 / ~ 16.93) regardless of SAE, class, or domain, indicating that SAE chiefly benefits learned-attribution methods. Further analyses are provided in Supplementary §1.4, Tables 2–5.

To validate that the proposed UMAP linear constraint effectively linearizes the attribution space and yields robust scores within tokenized features, we performed an additional PCA analysis. We extracted the top eight principal components and visualized the first two, which capture the majority of variance in the cohort distribution. Under the UMAP constraint, these components reveal an approximately linear structure along the dominant statistical

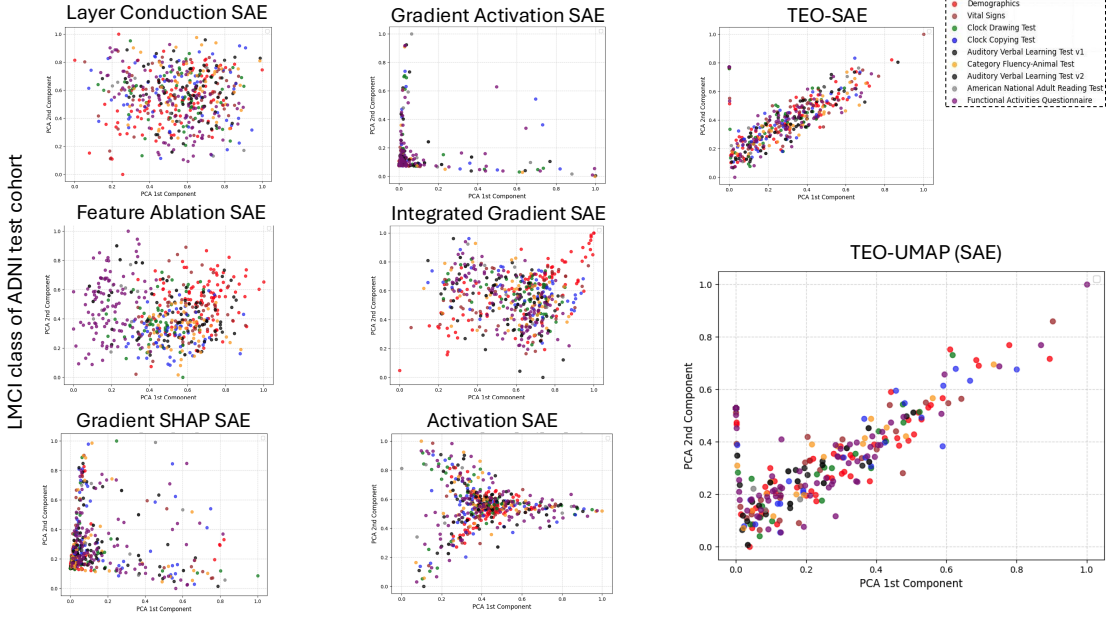


Figure 2: PCA of token-level attribution representations (LMCI, ADNI test set). The first two principal components are shown, computed from the top eight PCA components of the attribution matrix.

directions (Figure 2), inducing a coherent global organization of the feature space and promoting consistent population-level attribution patterns across subjects (Appendix B.3).

4.2 Individual- and Cohort-Level Quality of Explanations

Figure 3 presents qualitative local-level and cohort-level attributions for the LMCI class in the three-class classification task on both IID and OOD settings using our proposed optimisers TEO, TEO-SAE, and TEO-UMAP (SAE). At the local level, the heatmaps illustrate feature importance, with tokens colour-coded to indicate relevance (green = positive relevance; red = negative relevance). Visually, TEO-SAE produces the tightest, least noisy explanations—fewer spurious highlights and clearer token groupings—consistent with its lowest RIS/ROS in Table 1. Adding the UMAP constraint restores higher sparseness while preserving much of TEO-SAE stability: TEO-UMAP (SAE) yields compact, well-separated patterns that remain clinically interpretable across IID and OOD. Across classes and datasets, higher Sparseness corresponds to less diffuse maps with balanced positive/negative highlights, whereas low Sparseness with high RIS/ROS manifests as saturated red/green patches and unstable saliency (see Supplementary Figures 7–16). Among the six classical attribution methods (Activation, Layer Conductance, Feature Ablation, Gradient SHAP, Gradient Activation, Integrated Gradient), Feature Ablation attains the highest Sparseness but exhibits poorer stability (elevated RIS/ROS), a gap that worsens with SAE due to decoder-driven “decompression” (Supplementary Figures 7–8). Layer Conductance shows the opposite trade-off: SAE reduces Sparseness but improves stability (lower RIS/ROS), with similar stability gains observed for Gradient Activation, Integrated Gradient, and Gradient SHAP (Supplementary Figures 9–10). Overall, none of these classical methods match the proposed framework as TEO-SAE is consistently most stable, and TEO-UMAP (SAE) offers a tunable sparsity–stability compromise that generalises from ADNI to BrainLat (for extended analyses see Supplementary §1.6).

At the cohort level, we extracted UMAP embeddings to visualise patterns and text–category clusters in 2D space, observing any spreading effects or homogeneous clustering. We also applied PCA to identify high-contributing features (threshold 0.6 on the first component; Figure 3). Moving from TEO to TEO-SAE produces tighter, more homogeneous low-to-high attribution and the lowest RIS/ROS (highest stability), but also a marked reduction in sparseness, evident as broader token spread in the 2D manifold (see Figure 3). In some cases, this stabilisation concentrates signals so strongly that few features exceed the significance threshold (square box in the 1D scatter plot where PCA first component ≥ 0.6), and not all subgroups are represented (Figure 3, Supplementary Figure 32). Imposing a linear UMAP constraint (TEO-UMAP) mitigates this effect by restoring sparsity in significant attributions while retaining stability, yielding compact, clinically interpretable maps with more uniform subgroup coverage (Figure 3; Supplementary Figures 33–35). The behaviour of the proposed framework (TEO, TEO-SAE,

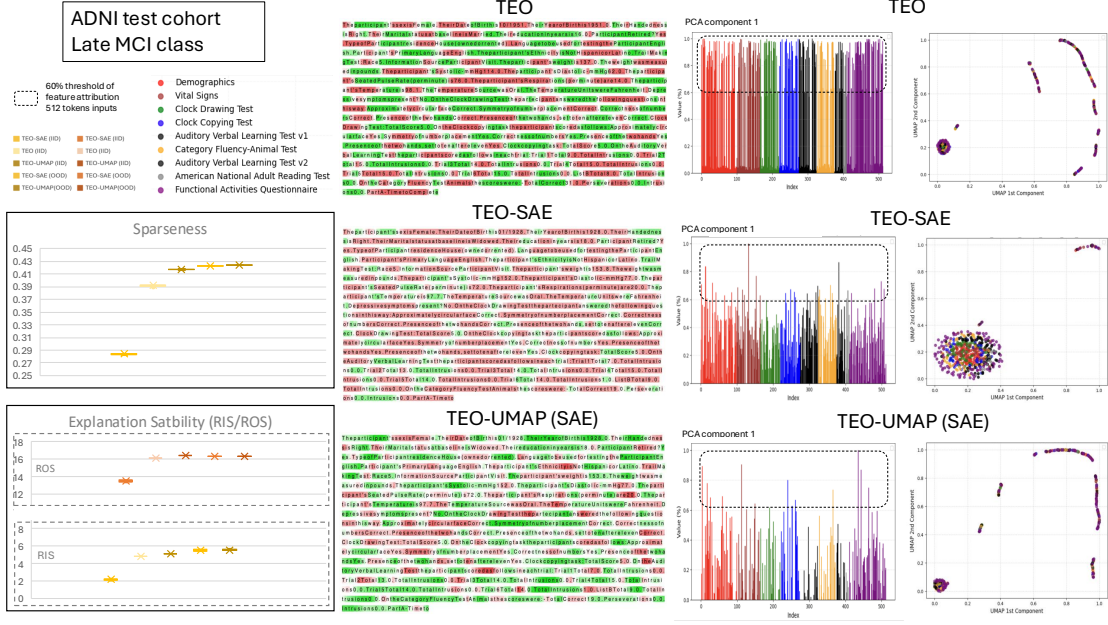


Figure 3: **Left:** Stability-sparsity frontier for explanation optimizers on ADNI (Late MCI) in the testing cohort. Scatter points show TEO, TEO-SAE, and TEO-UMAP (SAE) on ADNI (IID) and BrainLat (OOD). Metrics: Sparseness (higher is better) vs. RIS/ROS stability (lower is better). **Middle:** Token-level heatmap produced by the proposed framework, with feature-attribution scale (green: positive relevance; red: negative relevance; white: neutral). **Right:** 1st PCA and 2D UMAP projections of the full testing cohort. Thresholding uses 60% feature attribution over 512 tokens. The generated input text is split into nine subgroups (different colours) based on input modality, as detailed in Supplementary Material 1.1.5, for pattern analysis and biomarker identification.

TEO-UMAP) shows that higher sparseness corresponds to less diffuse, more balanced highlights, whereas lower sparseness with higher RIS/ROS results in saturated red/green patches. This mirrors the patterns observed across the six classical methods (Activation, Layer Conduction, Feature Ablation, Gradient SHAP, Gradient Activation, Integrated Gradient; Appendix A.2). With SAE, feature-learning explainers such as Layer Conduction generally gain stability (lower RIS/ROS) at some sparsity cost, while Feature Ablation maintains high sparsity but remains unstable. None, however, match the stability-sparsity trade-off achieved by TEO-SAE and TEO-UMAP (box plots in Figure 3; Table 1). Supplementary §1.7 (Figures 22–31) provides more details about cohort-level attributions.

4.3 Are Monosemantic Representation-Based Attribution Methods Statistically Distinct from Standard Attribution Techniques?

A statistical evaluation of interpretability metrics (sparseness, RIS, and ROS, see Supplementary §1.5) across methods with and without the SAE layer was computed. In the binary ADNI task, *paired t*-tests with FDR correction showed that adding an SAE bottleneck significantly reduced Complexity ($p < 10^{-10}$) and RIS ($p < 10^{-4}$) in both groups, while ROS changes were small and inconsistent (marginal for Control, non-significant for Alzheimer's). The strongest SAE effects appeared in attribution metrics, with Gradient SHAP ($p < 10^{-45}$), Layer Conduction ($p = 3.2 \times 10^{-7}$), Integrated Gradients ($p < 10^{-55}$), and the TEO ($p < 10^{-95}$) all showing decisive reductions, confirming robust stability gains under SAE. In the three-class ADNI task, *paired t*-tests and Wilcoxon signed-rank tests (BH-FDR) indicated that the MCI group showed the clearest improvement: ROS decreased strongly ($t(17) = -10.12$, $p = 1.30 \times 10^{-8}$; $W = 0$, $p = 8.0 \times 10^{-6}$, $q = 2.3 \times 10^{-5}$), RIS showed a smaller reduction detected non-parametrically ($W = 19$, $p = 0.00117$), and Complexity increased modestly by Wilcoxon ($W = 17$, $p = 7.9 \times 10^{-4}$) while paired *t*-tests were non-significant. Control and LMCI had incomplete pairs, preventing matched testing with correction. Overall, SAE reliably improves attribution stability (lower RIS/ROS) and increase sparseness in binary tasks, with the three-class MCI group showing the most consistent ROS gains.

4.4 Clinical Impact and Diagnostic Outcomes in Alzheimer's Disease

Biomarker Identification: Our findings demonstrate that both TEO-SAE and TEO-UMAP yield the most reliable and consistent identification of informative sources across the nine multimodal subgroups. Using a threshold of 0.6 on the first principal component (PCA; Figure 3), we observe systematic and class-specific biomarker patterns in the IID binary task (ADNI). For the Control group, TEO-SAE is primarily driven by FAQ, whereas TEO-UMAP shifts emphasis toward DEM, AVLT2, and FAQ. For the Alzheimer's group, TEO prioritises FAQ, AVLT1, and CFA, while TEO-UMAP highlights ANART, FAQ, and DEM. In the three-class setting, TEO identifies AVLT1, CDT, and ANART as most influential for Controls, while TEO-UMAP selects AVLT1, CDT, and CFA. For MCI, TEO assigns highest relevance to CCT, AVLT2, and FAQ, whereas TEO-UMAP favours AVLT2, ANART, and CFA. For LMCI, TEO elevates AVLT1, FAQ, and CDT, while TEO-UMAP elevates FAQ, ANART, and AVLT2. These trends are summarised in Appendix Table 2 (Section B.2), with acronym definitions provided in Sections 1.1.5 (Table 1).

Importantly, these results illustrate how our proposed mechanistic attribution framework can disentangle which demographic/vital features and, crucially, which cognitive assessments contribute most strongly to each diagnostic category. This is particularly relevant in clinical neuroscience, where cognitive tests are often time-consuming, resource-intensive, and susceptible to demographic or cultural bias. Our framework provides a principled approach for identifying the most informative cognitive biomarkers—such as AVLT, FAQ, CDT, and ANART—which have been repeatedly linked to early Alzheimer's progression in the literature [33], [34]. By pinpointing the minimal set of high-yield assessments for each classification task, the method supports more efficient screening pipelines, reduces clinical burden, and enables scalable application in larger cohorts where repeated or comprehensive testing is impractical.

5 External Evaluation of Clinically Coherent Explanations

Setup. To assess the clinical relevance of our attribution framework and, in particular, the contribution of the SAE layer in producing monosemantic and diagnostically coherent explanations, we performed an auxiliary evaluation across three cohorts (Binary ADNI, Binary BrainLAT, and three-class ADNI). For each test sample, we extracted the top 50% most influential token attributions from TEO without SAE, TEO with SAE, and TEO-UMAP, and constructed class-specific CSV files in which highlighted characters for each attribution method were arranged column-wise, with the full character sequence (including the CLS token) provided in the first column to ensure clear sample-level distinction. These CSVs were then presented to a large language model (ChatGPT-5.1 [35]) under a fixed prompting protocol to yield an external, model-agnostic assessment of the interpretability structure encoded by each explanation space.

Results. Across both binary tasks, all three attribution methods correctly identified the pathological Alzheimer's class; however, TEO without SAE consistently fixated on task artefacts (e.g., instruction counts or label-like patterns) rather than clinically meaningful biomarkers, whereas TEO-SAE and TEO-UMAP surfaced coherent neurocognitive indicators, demographic risk factors, and processing-speed impairments. In the more challenging three-class ADNI setting, the SAE-enabled variants again produced clearer diagnostic separation and more structured biomarker profiles, while TEO without SAE failed to identify pathology or highlight relevant clinical features. These results show that using an SAE-driven monosemantic representation substantially strengthens the reliability, diagnostic validity, and clinical interpretability of the resulting attribution signals (see Appendix B.1.; Figure 4).

6 Conclusion

We introduced a unified interpretability framework that combines monosemantic feature extraction with learning-based explanation optimization, optionally augmented with a geometry-aware constraint. Across IID and OOD settings and multiple classification tasks, the proposed methods yield more stable and robust explanations than classical attribution approaches, defining a tunable sparsity–stability trade-off that generalizes under distribution shift. Clinically, the framework identifies coherent diagnostic markers and enables low-dimensional cohort-level explanations that support efficient assessment. Overall, this approach advances robust and trustworthy interpretability for LLM-based Alzheimer's disease analysis.

Impact Statement

This paper presents work whose goal is to advance the field of machine learning. There are many potential societal consequences of our work, none of which we feel must be specifically highlighted here. The paper discusses several potential positive societal impacts, particularly emphasizing its relevance to clinical applications such as the early

diagnosis and treatment planning of Alzheimer's Disease. By proposing a unified interpretability framework that combines attributional and mechanistic techniques, the authors aim to enhance the trustworthiness, consistency, and human alignment of large language model (LLM) outputs. This improved interpretability is presented as a means to support safer and more effective integration of LLMs into cognitive health and clinical decision-making, with the potential to uncover clinically meaningful patterns and ultimately improve patient outcomes. However, the paper does not explicitly address possible negative societal impacts of the work. It does not discuss risks such as the misinterpretation of model ex-677 planations, over-reliance on machine-generated insights in high-stakes medical contexts, or the potential for the framework to inadvertently reinforce biases embedded in training data. Societal impacts can be better established through future work, in which we plan to incorporate clinician-in-the-loop evaluation and patients.

Acknowledgments

This acknowledgment complies with the dataset license and does not affect the anonymization of the authors. Data collection and sharing for the Alzheimer's Disease Neuroimaging Initiative (ADNI) is funded by the National Institute on Aging (National Institutes of Health Grant U19AG024904). The grantee organization is the àNorthern California Institute for Research and Education. Past funding was obtained from: the National Institute of Biomedical Imaging and Bioengineering, the Canadian Institutes of Health Research, and private sector contributions through the Foundation for the National Institutes of Health (FNIH) including generous contributions from the following: AbbVie, Alzheimer's Association; Alzheimer's Drug Discovery Foundation; Araclon Biotech; BioClinica, Inc.; Biogen; BristolMyers Squibb Company; CereSpir, Inc.; Cogstate; Eisai Inc.; Elan Pharmaceuticals, Inc.; Eli Lilly and Company; EuroImmun; F. Hoffmann-La Roche Ltd and its affiliated company Genentech, Inc.; Fujirebio; GE Healthcare; IXICO Ltd.; Janssen Alzheimer Immunotherapy Research & Development, LLC.; Johnson & Johnson Pharmaceutical Research & Development LLC.; Lumosity; Lundbeck; Merck & Co., Inc.; Meso Scale Diagnostics, LLC.; NeuroRx Research; Neurotrack Technologies; Novartis Pharmaceuticals Corporation; Pfizer Inc.; Piramal Imaging; Servier; Takeda Pharmaceutical Company; and Transition Therapeutics.

References

- [1] Finale Doshi-Velez and Been Kim. Towards a rigorous science of interpretable machine learning. *arXiv preprint arXiv:1702.08608*, 2017.
- [2] Haochen Liu, Yiqi Wang, Wenqi Fan, Xiaorui Liu, Yaxin Li, Shaili Jain, Yunhao Liu, Anil Jain, and Jiliang Tang. Trustworthy ai: A computational perspective. *ACM Trans. Intell. Syst. Technol.*, 14(1), November 2022.
- [3] Alireza A. Tahami Monfared, Melissa J. Byrnes, Lauren A. White, Jianwei Zhang, Eric Yu, and Jeng Lin. Alzheimer's disease: Epidemiology and clinical progression. *Neurology and Therapy*, 11:553–569, 2022.
- [4] Clifford R Jack et al. Nia-aa research framework: Toward a biological definition of alzheimer's disease. *Alzheimer's & Dementia*, 14(4):535–562, 2018.
- [5] Garam Lee, Kwangsik Nho, Byungkon Kang, Kyung-Ah Sohn, Dokyoon Kim, Michael W. Weiner, and Alzheimer's Disease Neuroimaging Initiative. Predicting alzheimer's disease progression using multi-modal deep learning approach. *Scientific Reports*, 9(1):1952, 2019.
- [6] Tom B Brown, Benjamin Mann, Nick Ryder, Melanie Subbiah, Jared Kaplan, Prafulla Dhariwal, Arvind Neelakantan, Pranav Shyam, Girish Sastry, Amanda Askell, et al. Language models are few-shot learners. In *Advances in neural information processing systems*, volume 33, pages 1877–1901, 2020.
- [7] Hugo Touvron et al. Llama 2: Open foundation and fine-tuned chat models. <https://ai.meta.com/llama/>, 2023.
- [8] Chris Olah, Arvind Satyanarayanan, Ludwig Schubert Wusser, and Shan Carter. Zoom in: An introduction to circuits. *Distill*, 2020.
- [9] Hoagy Cunningham, Aidan Ewart, Logan Riggs, Robert Huben, and Lee Sharkey. Sparse autoencoders find highly interpretable features in language models, 2023.
- [10] Nelson Elhage, Tristan Hume, Catherine Olsson, Nicholas Schiefer, Tom Henighan, Shauna Kravec, Zac Hatfield-Dodds, Robert Lasenby, Dawn Drain, Carol Chen, Roger Grosse, Sam McCandlish, Jared Kaplan, Dario Amodei, Martin Wattenberg, and Christopher Olah. Toy models of superposition, 2022.
- [11] Wojciech Samek, Grégoire Montavon, Sebastian Lapuschkin, Christopher J. Anders, and Klaus-Robert Müller. Explaining deep neural networks and beyond: A review of methods and applications. *Proceedings of the IEEE*, 109(3):247–278, 2021.

- [12] Bas H.M. van der Velden, Hugo J. Kuijf, Kenneth G.A. Gilhuijs, and Max A. Viergever. Explainable artificial intelligence (xai) in deep learning-based medical image analysis. *Medical Image Analysis*, 79:102470, 2022.
- [13] Gwenolé Quellec, Hassan Al Hajj, Mathieu Lamard, Pierre-Henri Conze, Pascale Massin, and Béatrice Cochener. Explain: Explanatory artificial intelligence for diabetic retinopathy diagnosis. *Medical Image Analysis*, 72:102118, 2021.
- [14] Michail Mamalakis, Krit Dwivedi, Michael Sharkey, Samer Alabed, David Kiely, and Andrew J. Swift. A transparent artificial intelligence framework to assess lung disease in pulmonary hypertension. *Scientific Reports*, 13(1):3812, 2023.
- [15] Michail Mamalakis, Antonios Mamalakis, Ingrid Agartz, Lynn Egeland Mørch-Johnsen, Graham K. Murray, John Suckling, and Pietro Lio. Solving the enigma: Enhancing faithfulness and comprehensibility in explanations of deep networks. *AI Open*, 6:70–81, 2025.
- [16] Liv Gorton. The missing curve detectors of inceptionv1: Applying sparse autoencoders to inceptionv1 early vision. *arXiv preprint arXiv:2406.03662*, 2024.
- [17] Scott M Lundberg and Su-In Lee. A unified approach to interpreting model predictions. *Advances in neural information processing systems*, 30, 2017.
- [18] Mukund Sundararajan, Ankur Taly, and Qiqi Yan. Axiomatic attribution for deep networks, 2017.
- [19] Leland McInnes, John Healy, and James Melville. Umap: Uniform manifold approximation and projection for dimension reduction. *arXiv preprint arXiv:1802.03426*, 2018.
- [20] Karl Pearson F.R.S. Liii. on lines and planes of closest fit to systems of points in space. *The London, Edinburgh, and Dublin Philosophical Magazine and Journal of Science*, 2(11):559–572, 1901.
- [21] Susanne G. Mueller, Michael W. Weiner, Leon J. Thal, Ronald C. Petersen, Clifford Jack, William Jagust, John Q. Trojanowski, Arthur W. Toga, and Laurel Beckett. The alzheimer's disease neuroimaging initiative. *Neuroimaging Clinics of North America*, 15(4):869–877, 2005. Alzheimer's Disease: 100 Years of Progress.
- [22] Pavel Prado, Vicente Medel, Agustín Sainz-Ballesteros, Hernando Santamaría-García, Sebastián Moguilner, Jhony Mejía, Raúl González-Gómez, Andrea Slachevsky, María Isabel Behrens, David Aguillón, Francisco Lopera, Mario A. Parra, Diana Matallana, Marcelo Adrián Maito, Adolfo M. García, Nilton Custodio, Alberto Ávila Funes, Stefanie Piña-Escudero, Agustina Birba, Sol Fittipaldi, Agustina Legaz, and Agustín Ibáñez. The brainlat project: a multimodal neuroimaging dataset of neurodegeneration from underrepresented backgrounds. *Scientific Data*, 10:889, 2023.
- [23] Scott M. Lundberg and Su-In Lee. A unified approach to interpreting model predictions. *CoRR*, abs/1705.07874, 2017.
- [24] Chirag Agarwal, Nari Johnson, Martin Pawelczyk, Satyapriya Krishna, Eshika Saxena, Marinka Zitnik, and Himabindu Lakkaraju. Rethinking stability for attribution-based explanations, 2022.
- [25] Prasad Chalasani, Jiefeng Chen, Amrita Roy Chowdhury, Xi Wu, and Somesh Jha. Concise explanations of neural networks using adversarial training. In Hal Daumé III and Aarti Singh, editors, *Proceedings of the 37th International Conference on Machine Learning (ICML)*, volume 119 of *Proceedings of Machine Learning Research*, pages 1383–1391, Virtual Event, online, July 13–18 2020. PMLR. Originally released as arXiv:1810.06583 (2018).
- [26] Olaf Ronneberger, Philipp Fischer, and Thomas Brox. U-net: Convolutional networks for biomedical image segmentation. In *International Conference on Medical Image Computing and Computer-Assisted Intervention (MICCAI)*, pages 234–241. Springer, 2015.
- [27] Ashish Vaswani, Noam Shazeer, Niki Parmar, Jakob Uszkoreit, Llion Jones, Aidan N. Gomez, Łukasz Kaiser, and Illia Polosukhin. Attention is all you need, 2017.
- [28] Toan Q. Nguyen and Julian Salazar. Transformers without tears: Improving the normalization of self-attention. *arxiv*, 2019.
- [29] Nelson Elhage, Neel Nanda, et al. A mechanistic interpretability analysis of superposition in neural networks. *Transformer Circuits Thread*, 2022.
- [30] Wes Gurnee and Max Tegmark. Language models represent space and time, 2024.
- [31] Joseph Bloom, Curt Tigges, Anthony Duong, and David Chanin. Saelens. <https://github.com/jbloomAus/SAELens>, 2024.

- [32] Anna Hedström, Leander Weber, Daniel Krakowczyk, Dilyara Bareeva, Franz Motzkus, Wojciech Samek, Sebastian Lapuschkin, and Marina Marina M.-C. Höhne. Quantus: An explainable ai toolkit for responsible evaluation of neural network explanations and beyond. *Journal of Machine Learning Research*, 24(34):1–11, 2023.
- [33] Ronald C. Petersen, Glenn E. Smith, Susan C. Waring, Robert J. Ivnik, Eric G. Tangalos, and Emre Kokmen. Mild cognitive impairment: clinical characterization and outcome. *Archives of Neurology*, 56(3):303–308, 1999.
- [34] Mark W. Bondi, Emily C. Edmonds, Amy J. Jak, Lindsay R. Clark, Lisa Delano-Wood, Carrie R. McDonald, Daniel A. Nation, David J. Libon, Rhoda Au, Douglas Galasko, and David P. Salmon and. Neuropsychological criteria for mild cognitive impairment improves diagnostic precision, biomarker associations, and progression rates. *Journal of Alzheimer's Disease*, 42(1):275–289, 2014. PMID: 24844687.
- [35] OpenAI. ChatGPT-4o. <https://openai.com/chatgpt>, 2024. Accessed May 2025.
- [36] Jonathan Ho, Ajay Jain, and Pieter Abbeel. Denoising diffusion probabilistic models. *arXiv preprint arXiv:2006.11239*, 2020.
- [37] Rodrigo Quiroga et al. Invariant visual representation by single neurons in the human brain. *Nature*, 435(7045):1102–1107, 2005.
- [38] Mattia Rigotti, Omri Barak, Melissa Warden, et al. The importance of mixed selectivity in complex cognitive tasks. *Nature*, 497(7451):585–590, 2013.
- [39] Chris Olah, Nick Cammarata, Ludwig Schubert, Gabriel Goh, Michael Petrov, and Shan Carter. Zoom in: An introduction to circuits. *Distill*, 5(3):e00024.001, 2020.
- [40] Samuel Marks, Can Rager, Eric J Michaud, Yonatan Belinkov, David Bau, and Aaron Mueller. Sparse feature circuits: Discovering and editing interpretable causal graphs in language models. *arXiv preprint arXiv:2403.19647*, 2024.
- [41] Callum McDougall. Sae visualizer, 2024.
- [42] Trenton Bricken, Adly Templeton, Joshua Batson, Brian Chen, Adam Jermyn, Tom Conerly, Nick Turner, Cem Anil, Carson Denison, Amanda Askell, et al. Towards monosemanticity: Decomposing language models with dictionary learning. *Transformer Circuits Thread*, 2023.
- [43] Steven Bills, Nick Cammarata, Dan Mossing, Henk Tillman, Leo Gao, Gabriel Goh, Ilya Sutskever, Jan Leike, Jeff Wu, and William Saunders. Language models can explain neurons in language models. *openaipublic*, 2023.
- [44] Adly Templeton, Tom Conerly, Jonathan Marcus, Jack Lindsey, Trenton Bricken, Brian Chen, Adam Pearce, Craig Citro, Emmanuel Ameisen, Andy Jones, et al. Scaling monosemanticity: Extracting interpretable features from claude 3. *Transformer Circuits Thread*, 2024.
- [45] Senthooran Rajamanoharan, Arthur Conmy, Lewis Smith, Tom Lieberum, Vikrant Varma, János Kramář, Rohin Shah, and Neel Nanda. Improving dictionary learning with gated sparse autoencoders, 2024.
- [46] Leonard Bereska and Efstratios Gavves. Mechanistic interpretability for ai safety – a review, 2024.
- [47] Marco Túlio Ribeiro, Sameer Singh, and Carlos Guestrin. "why should i trust you?": Explaining the predictions of any classifier, 2016.
- [48] Sebastian Bach, Alexander Binder, Grégoire Montavon, Frederick Klauschen, Klaus-Robert Müller, and Wojciech Samek. On pixel-wise explanations for non-linear classifier decisions by layer-wise relevance propagation. *PLOS ONE*, 10(7):1–46, 07 2015.
- [49] Amitojdeep Singh, Sourya Sengupta, and Vasudevan Lakshminarayanan. Explainable deep learning models in medical image analysis, 2020.
- [50] Patrick Kolpaczki, Viktor Bengs, Maximilian Muschalik, and Eyke Hüllermeier. Approximating the shapley value without marginal contributions, 2024.
- [51] Nelson Elhage, Tristan Hume, Catherine Olsson, Nicholas Schiefer, Tom Henighan, Shauna Kravec, Zac Hatfield-Dodds, Robert Lasenby, Dawn Drain, Carol Chen, Roger Grosse, Sam McCandlish, Jared Kaplan, Dario Amodei, Martin Wattenberg, and Christopher Olah. Toy models of superposition, 2022.
- [52] Catherine Olsson, Nelson Elhage, Neel Nanda, Nicholas Joseph, Nova DasSarma, Tom Henighan, Ben Mann, Amanda Askell, Yuntao Bai, Anna Chen, et al. In-context learning and induction heads. *Transformer Circuits Thread*, 2022.

A Technical Appendices

A.1 Attributational theory and methods

Attribution explainability methods follow the framework of additive feature attribution, where the explanation model $g(f, \mathbf{x})$ is represented as a linear function of simplified input features:

$$g(f, \mathbf{x}) = \phi_0 + \sum_{i=1}^M \phi_i x_i \quad (7)$$

Here, f is the predictive model, $\phi_i \in \mathbb{R}$ is the attribution (importance) assigned to feature x_i , and M is the number of simplified input features.

For this study, we employed six well-established attributional interpretability methods applied to large language models (LLMs), denoted as $K = 6$: *Feature Ablation*, *Layer Activations* (which capture the embedding activation space of a specific layer of interest within the LLM), *Layer DeepLIFT SHAP*, *Layer Gradient SHAP* [23], *Layer Integrated Gradients* [18], and *Layer Gradient \times Activation*.

To align these layer-wise interpretability methods with the additive feature attribution framework, we reinterpret the internal activations (i.e., latent units) of a network layer L as simplified input features. The objective is to estimate an attribution score ϕ_i for each unit, where $\phi_i \in \mathbb{R}$ quantifies the contribution of the corresponding neuron to the model's prediction.

Layer SHAP implementations: This directly corresponds to the Shapley formulation:

$$\phi_i = \sum_{S \subseteq F \setminus \{i\}} \frac{|S|!(|F| - |S| - 1)!}{|F|!} [f_{S \cup \{i\}}(x_{S \cup \{i\}}) - f_S(x_S)] \quad (8)$$

In practice, Deep SHAP approximates this using sampling and a chain-rule based linearization over network layers [23]. *Gradient SHAP* assumes that input features are independent and that the explanation model is linear, allowing explanations to be expressed as an additive composition of feature contributions. Under these assumptions, SHAP values [23] can be approximated by computing the expected gradients over a distribution of perturbed inputs. Specifically, Gaussian noise is added to each input feature to generate multiple baseline samples, and the resulting gradients are averaged to approximate SHAP attributions.

Activation Attribution: This method treats the raw activation $a_i^L(\mathbf{x})$ as proportional to its importance in the output. In the additive form:

$$\phi_i = a_i^L(\mathbf{x}) \quad (9)$$

Assuming linearity between layer L and the output, activations themselves serve as proxy contributions.

Gradient \times Activation Attribution: This method computes the element-wise product between the activation values and the gradients of the model output with respect to those activations, thereby capturing the first-order sensitivity of the output to the neurons in the layer. To this end, the method estimates the first-order sensitivity of the output with respect to the activation:

$$\phi_i = a_i^L(\mathbf{x}) \cdot \frac{\partial f}{\partial a_i^L}(\mathbf{x}) \quad (10)$$

This corresponds to a local linear approximation (first-order Taylor expansion) of the model at \mathbf{x} , akin to DeepLIFT and the SHAP linearization used in DeepLIFT SHAP [23].

Feature Ablation Attribution: This attributional interpretability technique is a perturbation-based approach to estimating attributions. It involves replacing the input or output values of a selected layer with a given baseline or reference value and computing the resulting change in the model's output. By default, each neuron (i.e., scalar input or output value) within the layer is ablated independently. For neuron group $S \subseteq \{1, \dots, d_L\}$, the perturbed activation is:

$$\tilde{a}_i^L = \begin{cases} b_i^L & \text{if } i \in S, \\ a_i^L(\mathbf{x}) & \text{otherwise,} \end{cases} \quad (11)$$

and the attribution is the marginal effect:

$$\phi_S = f(\mathbf{x}; \tilde{\mathbf{a}}_S^L) - f(\mathbf{x}) \quad (12)$$

All attribution methods were applied to the final (22nd) layer of the MODERN-BERT LLM—the model variant that achieved the highest classification accuracy in our evaluations (see Supplementary material section 1.1). These formulations allow us to ground various neural attribution techniques within a unified additive explanation model, facilitating their comparison and hybridization under shared theoretical assumptions.

A.2 Attributional explanation optimizer framework

Let $\mathcal{A} = \{A_1, A_2, \dots, A_K\}$ denote the set of $K = 6$ attribution methods applied to the final layer L of the model f . Each method A_k generates an attribution vector $\boldsymbol{\phi}^{(k)} = [\phi_1^{(k)}, \phi_2^{(k)}, \dots, \phi_M^{(k)}]$, where M is the number of latent features (neurons) in layer L . The goal is to derive a unified attribution vector $\tilde{\boldsymbol{\phi}}$ that captures the consensus explanation across methods.

A.2.1 Scoring and Weighting Attribution Methods

Each attribution vector $\boldsymbol{\phi}^{(k)}$ is evaluated using the following quality metrics:

A.2.2 Evaluation Interpretability Metrics

We evaluate the robustness of each attribution method A_k using the following stability metrics:

Relative Input Stability (RIS):

$$M_{\text{RIS}}^{(k)} = \text{RIS}(f, \boldsymbol{\phi}^{(k)}; \mathbf{x}) = \frac{\|\mathbf{x}\|_p}{\|\boldsymbol{\phi}^{(k)}(\mathbf{x})\|_p} \max_{\mathbf{x}' \in \mathcal{N}_{\mathbf{x}}, \hat{y}_{\mathbf{x}'} = \hat{y}_{\mathbf{x}}} \frac{\|\boldsymbol{\phi}^{(k)}(\mathbf{x}) - \boldsymbol{\phi}^{(k)}(\mathbf{x}')\|_p}{\|\mathbf{x} - \mathbf{x}'\|_p} \quad (13)$$

Relative Output Stability (ROS):

$$M_{\text{ROS}}^{(k)} = \text{ROS}(f, \boldsymbol{\phi}^{(k)}; \mathbf{x}) = \frac{\|f(\mathbf{x})\|_p}{\|\boldsymbol{\phi}^{(k)}(\mathbf{x})\|_p} \max_{\mathbf{x}' \in \mathcal{N}_{\mathbf{x}}, \hat{y}_{\mathbf{x}'} = \hat{y}_{\mathbf{x}}} \frac{\|\boldsymbol{\phi}^{(k)}(\mathbf{x}) - \boldsymbol{\phi}^{(k)}(\mathbf{x}')\|_p}{\|f(\mathbf{x}) - f(\mathbf{x}')\|_p} \quad (14)$$

Here, $\mathcal{N}_{\mathbf{x}}$ denotes a neighborhood of perturbed inputs \mathbf{x}' around \mathbf{x} , and $\hat{y}_{\mathbf{x}}$ is the predicted class label. Both metrics measure the relative sensitivity of the attribution vector $\boldsymbol{\phi}^{(k)}$ to perturbations in the input or output space.

Sparseness Metric: We quantify the **sparseness** of the attribution vector $\boldsymbol{\phi}^{(k)} \in \mathbb{R}^d$ using the *Gini Index*, a measure of inequality that has been shown to satisfy several desirable properties for evaluating sparseness [25]. This formulation is adopted in the context of explaining neural network predictions [25].

Let $\nu \in \mathbb{R}_{\geq 0}^d$ be a non-negative vector. Denote by $\nu_{(k)}$ the k -th smallest element in ν after sorting it in non-decreasing order. Then, the **Gini Index** $G(\nu) \in [0, 1]$ is defined as:

$$G(\nu) = 1 - 2 \sum_{k=1}^d \frac{\nu_{(k)}}{\|\nu\|_1} \cdot \left(\frac{d-k+0.5}{d} \right), \quad (15)$$

where $\|\nu\|_1 = \sum_{i=1}^d \nu_i$ is the ℓ_1 -norm of ν . To evaluate the sparseness of an attribution vector $\boldsymbol{\phi}^{(k)}$, we apply the Gini Index to the vector of its absolute values:

$$\text{Sparseness}(\boldsymbol{\phi}^{(k)}) = G(|\boldsymbol{\phi}^{(k)}|),$$

where $|\boldsymbol{\phi}^{(k)}| = (|\phi_1^{(k)}|, |\phi_2^{(k)}|, \dots, |\phi_d^{(k)}|)$.

Higher values of $G(|\boldsymbol{\phi}^{(k)}|)$ indicate greater sparseness. In the extreme case, if only one component is non-zero, the Gini Index reaches its maximum value of 1, indicating perfect sparseness. If all components are equal, the Gini Index is 0.

A.2.3 Aggregation of Attributions

The weighted average attribution vector $\bar{\phi}$ is calculated as:

$$\bar{\phi} = \sum_{k=1}^K w_k \cdot \phi^{(k)} \quad (16)$$

This vector serves as the target explanation for the optimization process.

A.2.4 Explanation Reconstruction via Encoder–Decoder Models

An encoder–decoder model is trained to generate a reconstructed explanation $\hat{\phi}$ from the original input x . Two architectures are considered the Diffusion UNet1D [26] and the x-transformer autoencoder [27, 28].

Diffusion model: The diffusion model follows the basic structure of a 1-dimensional U-Net and is trained using diffusion principles. In this framework, diffusion models [36] are latent variable models in which the observed data $\phi_0^{(k)}$ is gradually corrupted through a forward noising process, producing a sequence of latent variables $\phi_{1:T}^{(k)}$. A corresponding reverse process is then learned to recover the original data from noise. The mathematical formulation is as follows:

FORWARD PROCESS: A fixed Markov chain progressively adds Gaussian noise to the data:

$$q(\phi_{1:T}^{(k)} | \phi_0^{(k)}) := \prod_{t=1}^T q(\phi_t^{(k)} | \phi_{t-1}^{(k)}), \quad q(\phi_t^{(k)} | \phi_{t-1}^{(k)}) := \mathcal{N}(\phi_t^{(k)}; \sqrt{1 - \beta_t} \phi_{t-1}^{(k)}, \beta_t \mathbf{I}) \quad (17)$$

Alternatively, sampling from the forward process at an arbitrary timestep t is possible in closed form:

$$q(\phi_t^{(k)} | \phi_0^{(k)}) = \mathcal{N}(\phi_t^{(k)}; \sqrt{\bar{\alpha}_t} \phi_0^{(k)}, (1 - \bar{\alpha}_t) \mathbf{I}), \quad (18)$$

where $\alpha_t := 1 - \beta_t$ and $\bar{\alpha}_t := \prod_{s=1}^t \alpha_s$.

REVERSE PROCESS: A learned time-reversal model with Gaussian transitions:

$$p_\theta(\phi_{0:T}^{(k)}) := p(\phi_T^{(k)}) \prod_{t=1}^T p_\theta(\phi_{t-1}^{(k)} | \phi_t^{(k)}), \quad p_\theta(\phi_{t-1}^{(k)} | \phi_t^{(k)}) := \mathcal{N}(\phi_{t-1}^{(k)}; \mu_\theta(\phi_t^{(k)}, t), \Sigma_\theta(\phi_t^{(k)}, t)), \quad (19)$$

where $p(\phi_T^{(k)}) := \mathcal{N}(\phi_T^{(k)}; \mathbf{0}, \mathbf{I})$.

TRAINING OBJECTIVE: The training objective of diffusion models is based on a variational bound, which includes Kullback–Leibler (KL) divergence terms. The KL term comparing the true posterior from the forward process and the model's learned reverse process is written as:

$$\text{KL}\left(q(\phi_{t-1}^{(k)} | \phi_t^{(k)}, \phi_0^{(k)}) \| p_\theta(\phi_{t-1}^{(k)} | \phi_t^{(k)})\right) \quad (20)$$

Both distributions are Gaussian:

$$q(\phi_{t-1}^{(k)} | \phi_t^{(k)}, \phi_0^{(k)}) = \mathcal{N}(\phi_{t-1}^{(k)}; \tilde{\mu}_t(\phi_t^{(k)}, \phi_0^{(k)}), \tilde{\beta}_t \mathbf{I}) \quad (21)$$

$$p_\theta(\phi_{t-1}^{(k)} | \phi_t^{(k)}) = \mathcal{N}(\phi_{t-1}^{(k)}; \mu_\theta(\phi_t^{(k)}, t), \sigma_t^2 \mathbf{I}) \quad (22)$$

The closed-form KL divergence between two Gaussians $\mathcal{N}(\mu_1, \sigma_1^2 \mathbf{I})$ and $\mathcal{N}(\mu_2, \sigma_2^2 \mathbf{I})$ in d -dimensions is:

$$\text{KL} = \frac{1}{2} \left[\log\left(\frac{\sigma_2^2}{\sigma_1^2}\right) + \frac{\sigma_1^2 + \|\mu_1 - \mu_2\|^2}{\sigma_2^2} - d \right] \quad (23)$$

In our setting, this term is computed for each timestep t and summed across all steps:

$$\mathcal{L}_{1:T-1} = \sum_{t=2}^T \mathbb{E}_{q(\phi_0^{(k)}, \phi_t^{(k)})} \left[\text{KL}\left(q(\phi_{t-1}^{(k)} | \phi_t^{(k)}, \phi_0^{(k)}) \| p_\theta(\phi_{t-1}^{(k)} | \phi_t^{(k)})\right) \right] \quad (24)$$

This forms a core part of the evidence lower bound (ELBO) optimized during training. Using variational inference, we minimize the negative ELBO:

$$\mathcal{L} = \mathbb{E}_q \left[-\log p(\phi_T^{(k)}) + \sum_{t=1}^T \text{KL} \left(q(\phi_{t-1}^{(k)} | \phi_t^{(k)}, \phi_0^{(k)}) \| p_\theta(\phi_{t-1}^{(k)} | \phi_t^{(k)}) \right) - \log p_\theta(\phi_0^{(k)} | \phi_1^{(k)}) \right]. \quad (25)$$

Each KL term compares Gaussian distributions and can be computed in closed form. The posterior $q(\phi_{t-1}^{(k)} | \phi_t^{(k)}, \phi_0^{(k)})$ is also Gaussian:

$$q(\phi_{t-1}^{(k)} | \phi_t^{(k)}, \phi_0^{(k)}) = \mathcal{N}(\phi_{t-1}^{(k)}; \tilde{\mu}_t(\phi_t^{(k)}, \phi_0^{(k)}), \tilde{\beta}_t \mathbf{I}), \quad (26)$$

with:

$$\tilde{\mu}_t(\phi_t^{(k)}, \phi_0^{(k)}) = \frac{\sqrt{\bar{\alpha}_{t-1}} \beta_t}{1 - \bar{\alpha}_t} \phi_0^{(k)} + \frac{\sqrt{\alpha_t} (1 - \bar{\alpha}_{t-1})}{1 - \bar{\alpha}_t} \phi_t^{(k)}, \quad (27)$$

$$\tilde{\beta}_t = \frac{1 - \bar{\alpha}_{t-1}}{1 - \bar{\alpha}_t} \beta_t. \quad (28)$$

SIMPLIFIED TRAINING LOSS: The common parameterization rewrites the objective as denoising score matching:

$$\mathcal{L}_{\text{simple}}(\theta) := \mathbb{E}_{t, \phi_0^{(k)}, \epsilon} \left[\left\| \epsilon - \epsilon_\theta(\sqrt{\bar{\alpha}_t} \phi_0^{(k)} + \sqrt{1 - \bar{\alpha}_t} \epsilon, t) \right\|^2 \right], \quad (29)$$

where $\epsilon \sim \mathcal{N}(0, \mathbf{I})$ and ϵ_θ is the neural network trained to predict noise.

In our implementation we compute the total loss for the diffusion model as:

$$\mathcal{L}_{\text{similarity}}(\hat{\phi}, \bar{\phi}) = \mathcal{L}_{\text{similarity}}(\theta) = \frac{1}{K+1} \sum_{l=0}^K \mathcal{L}_{\text{simple}}^{(l)}(\theta) \quad (30)$$

x-Transformer: Let the input sequence be:

$$\phi^{(k)} = [\phi_1^{(k)}, \phi_2^{(k)}, \dots, \phi_T^{(k)}] \in \mathbb{R}^{T \times d_{\text{in}}}$$

where $d_{\text{in}} = 7$ is the input dimensionality and $T = 512$ is the sequence length. We consider a Transformer-based encoder-decoder architecture operating on input sequences $\Phi^{(k)} \in \mathbb{R}^{B \times T \times d_{\text{in}}}$ at diffusion step k , where: B is the batch size, T is the sequence length, d_{in} is the input feature dimension, and $\Phi^{(k)}$ is the input sequence at step k .

The processing pipeline is mathematically formulated as follows:

INPUT PROJECTION AND POSITIONAL ENCODING: We first project the input to the model dimension d and add positional encodings:

$$\mathbf{X}_0 = \mathbf{W}_{\text{in}} \Phi^{(k)} + \mathbf{P}, \quad \mathbf{X}_0 \in \mathbb{R}^{B \times T \times d} \quad (31)$$

where: $\mathbf{W}_{\text{in}} \in \mathbb{R}^{d_{\text{in}} \times d}$ is a learnable linear projection matrix, and $\mathbf{P} \in \mathbb{R}^{1 \times T \times d}$ is a learnable positional embedding matrix.

ENCODER: MULTI-HEAD SELF-ATTENTION LAYERS: The encoder consists of L_e stacked multi-head self-attention (MHSA) layers:

$$\mathbf{H}_{\text{enc}} = \text{MHSA}_{L_e} \circ \dots \circ \text{MHSA}_1(\mathbf{X}_0) \quad (32)$$

where each MHSA layer performs:

$$\text{MHSA}(\mathbf{X}) = \text{Softmax} \left(\frac{\mathbf{Q} \mathbf{K}^\top}{\sqrt{d_h}} \right) \mathbf{V} \quad (33)$$

with: $\mathbf{Q}, \mathbf{K}, \mathbf{V}$: Query, Key, and Value matrices obtained via learned linear projections, and d_h : the dimensionality of each attention head.

DECODER INPUT PROJECTION: During training, the decoder may receive the ground-truth output $\Phi_{\text{target}}^{(k)} \in \mathbb{R}^{B \times T \times 1}$:

$$\mathbf{Y}_0 = \mathbf{W}_{\text{dec}} \Phi_{\text{target}}^{(k)} + \mathbf{P} \quad (34)$$

where $\mathbf{W}_{\text{dec}} \in \mathbb{R}^{1 \times d}$ is a projection matrix.

If no decoder input is available (e.g., during inference), $\Phi_{\text{target}}^{(k)}$ is initialized to a zero tensor.

DECODER MHSA + CROSS-ATTENTION LAYERS: The decoder consists of L_d layers of MHSA followed by cross-attention (CA) using the encoder context:

$$\mathbf{H}_{\text{dec}} = \text{CA}_{L_d} \circ \dots \circ \text{CA}_1 (\text{MHSA}_{L_d} \circ \dots \circ \text{MHSA}_1(\mathbf{Y}_0) \mid \mathbf{H}_{\text{enc}}) \quad (35)$$

Each cross-attention (CA) layer uses the decoder hidden state as the query and encoder output as the key and value:

$$\text{CA}(\mathbf{Y}, \mathbf{H}_{\text{enc}}) = \text{Softmax} \left(\frac{\mathbf{Q}_{\text{dec}} \mathbf{K}_{\text{enc}}^T}{\sqrt{d_h}} \right) \mathbf{V}_{\text{enc}} \quad (36)$$

OUTPUT PROJECTION: Finally, the decoder output is projected back to the target dimension:

$$\hat{\Phi}^{(k)} = \mathbf{W}_{\text{out}} \mathbf{H}_{\text{dec}}, \quad \hat{\Phi}^{(k)} \in \mathbb{R}^{B \times T \times 1} \quad (37)$$

where $\mathbf{W}_{\text{out}} \in \mathbb{R}^{d \times 1}$ is a linear projection matrix.

The similarity cost function is given by the Mean Squared Error (MSE) loss between the predicted output of the x-Transformer and the target weighted attribution vector as follow:

$$\mathcal{L}_{\text{similarity}}(\hat{\Phi}, \bar{\Phi}) = \mathcal{L}_{\text{MSE}} = \frac{1}{T} \sum_{t=1}^T \|\hat{\Phi}_t - \bar{\Phi}_t\|^2, \quad (38)$$

A.3 The total cost function of the optimizer

As previously highlighted, the reconstruction of the optimal explanation and the associated cost function adhere to the same principles and architectural design outlined in [15]. The cost function consists of three key components: sparseness, as defined in [25]; ROS and RIS scores [24]; and similarity. The integration of these components ensures a robust and interpretable evaluation. The total cost function for training the reconstruction model is:

$$\begin{aligned} \mathcal{L}_{\text{total}}(\Phi^{(k)}, \hat{\Phi}) = & \lambda_1 \cdot \frac{1}{M_{\text{RIS}}(f, \hat{\Phi})} + \lambda_2 \cdot \frac{1}{M_{\text{ROS}}(f, \hat{\Phi})} \\ & + \lambda_3 \cdot M_{\text{sparse}}(f, \hat{\Phi}) + \lambda_4 \cdot \mathcal{L}_{\text{similarity}}(\hat{\Phi}, \bar{\Phi}) \end{aligned} \quad (39)$$

where: $\lambda_1, \lambda_2, \lambda_3, \lambda_4$ are hyperparameters controlling the influence of each loss term. This formulation enables a principled and quantitative integration of multiple attribution methods, optimizing toward a robust and interpretable explanation.

A.4 The UMAP extraction and the linear constrain

Given a dataset $\hat{\Phi} = \{\hat{\Phi}_1, \hat{\Phi}_2, \dots, \hat{\Phi}_n\} \subset \mathbb{R}^D$, UMAP aims to find a low-dimensional embedding $U = \{u_1, u_2, \dots, u_n\} \subset \mathbb{R}^d$ where typically $d = 2$ or $d = 3$, such that the local topological structure of the data in $\hat{\Phi}$ is preserved in U .

HIGH-DIMENSIONAL GRAPH CONSTRUCTION: First, the algorithm constructs a k-nearest neighbors graph in the high-dimensional space $\hat{\Phi}$. The distance metric used to calculate the pairwise distances is typically Euclidean:

$$d(\hat{\Phi}_i, \hat{\Phi}_j) = \|\hat{\Phi}_i - \hat{\Phi}_j\|_2$$

Next, a conditional probability is defined between points $\hat{\Phi}_i$ and $\hat{\Phi}_j$ using a Gaussian distribution:

$$p_{ij} = \exp \left(-\frac{\|\hat{\Phi}_i - \hat{\Phi}_j\|^2}{\sigma_i^2} \right)$$

where σ_i is the bandwidth for the Gaussian distribution, determined through a binary search to match a fixed perplexity.

The graph is symmetrized:

$$P_{ij} = \frac{p_{ij} + p_{ji}}{2}$$

LOW-DIMENSIONAL EMBEDDING GRAPH: In the low-dimensional space, a similar probability is defined between points u_i and u_j :

$$q_{ij} = \frac{1}{1 + a\|u_i - u_j\|^{2b}}$$

where a and b are hyperparameters that control the shape of the distribution, and $\|u_i - u_j\|_2$ is the Euclidean distance between points in the low-dimensional embedding.

OBJECTIVE FUNCTION: The optimization process involves minimizing the cross-entropy between the high-dimensional and low-dimensional probability distributions:

$$\mathcal{L} = \sum_{i < j} [P_{ij} \log(Q_{ij}) + (1 - P_{ij}) \log(1 - Q_{ij})]$$

This loss function encourages points that are close in the high-dimensional space to be close in the low-dimensional space, and points that are distant to remain distant.

OPTIMIZATION PROCESS: The optimization is carried out using stochastic gradient descent (SGD), updating the embedding points $\{u_i\}$ iteratively based on the gradient of the loss function \mathcal{L} . The gradient updates for the low-dimensional embedding u_i are computed as follows:

$$\frac{\partial \mathcal{L}}{\partial u_i} = - \sum_{j \neq i} (P_{ij} - Q_{ij}) \frac{u_i - u_j}{\|u_i - u_j\|_2^2}$$

REGULARIZATION CONSTRAINT: To prevent the embedding from collapsing to a single point, we introduce a variance constraint to ensure that the variance of the embedding does not approach zero:

$$\text{Var}(U) = \frac{1}{n} \sum_{i=1}^n \|u_i - \bar{u}\|_2^2 \geq \epsilon$$

where $\bar{U} = \frac{1}{n} \sum_{i=1}^n u_i$ is the mean of the embeddings, and $\epsilon > 0$ is a small constant that enforces a lower bound on the variance.

APPLICATION OF UMAP IN OUR PROBLEM: To obtain a comparable low-dimensional representation of the attribution scores across all tokenizer features, we applied a feature-wise UMAP projection procedure to the normalized attribution matrix. For each attribution method, the attribution tensor has shape $\mathbb{R}^{M \times T}$, where M denotes the number of test samples in the evaluation cohort and T corresponds to the dimensionality of the tokenizer embedding space of the input text. For each feature $j \in \{1, \dots, T\}$, we first applied min–max normalization to the feature-specific attribution vector

$$\mathbf{x}^{(j)} \in \mathbb{R}^M,$$

and subsequently performed a one-dimensional UMAP projection to obtain a two-dimensional embedding

$$\mathbf{y}^{(j)} \in \mathbb{R}^{M \times 2}.$$

The resulting coordinates were then normalized to the interval $[0, 1]$ to ensure that all feature-wise embeddings share a common bounded range. This procedure preserves the relative neighborhood structure of the M -sample attribution distribution for each feature while mapping all T features into a comparable two-dimensional representation space.

The motivation for applying UMAP independently to each of the T tokenizer features is to ensure that all attribution methods are projected into an aligned and comparable representation space. Since each attribution method produces values defined over the same token embedding dimensions, a feature-wise nonlinear projection enables consistent cross-method comparison of attribution patterns within the shared tokenizer feature space.

LINEAR CONSTRAINT FOR EQUAL COMPONENTS IN UMAP: Let $u_i = (u_{i1}, u_{i2}, \dots, u_{id})$ denote the embedding of the i -th data point in a d -dimensional space. The requirement that the first and second embedding components are equal can be written as:

$$u_{i1} = u_{i2} \quad \forall i \in \{1, 2, \dots, n\}.$$

Equivalently, this can be expressed as the linear equality constraint:

$$u_{i1} - u_{i2} = 0 \quad \forall i \in \{1, 2, \dots, n\}.$$

This constraint enforces that, for each data point i , the first and second coordinates of the embedding vector u_i are identical.

Within the total objective $\mathcal{L}_{\text{total}}(\phi^{(k)}, \hat{\phi})$ of Eq. 35, an additional penalty term may be introduced to enforce this constraint. The penalty can be written as:

$$\lambda_5 \sum_{i=1}^n (u_{i1} - u_{i2})^2,$$

where λ_5 is a regularization parameter controlling the strength of the constraint. This term encourages the first and second components of each reconstructed embedding point from the optimizer $(\hat{\phi})$ to be equal, while still allowing flexibility depending on the value of λ_5 .

A.5 The superposition and the monosemantic representations

We model an embedding space as a real vector space \mathbb{R}^d , where a hidden activation vector $\mathbf{h} \in \mathbb{R}^d$ represents a combination of underlying semantic features. By the linear representation hypothesis, each interpretable feature corresponds to a fixed direction in \mathbb{R}^d [8, 29].

Let $\mathbf{a} \in \mathbb{R}^F$ be a sparse feature activation vector and $W \in \mathbb{R}^{d \times F}$ be a linear transformation such that:

$$\mathbf{h} = W\mathbf{a} = \sum_{i=1}^F a_i \mathbf{w}_i,$$

where \mathbf{w}_i denotes the i -th column of W , corresponding to the direction of the feature i .

If $F > d$, the map W cannot be invertible, and thus different combination of characteristics can map to the same embedding. This gives rise to superposition, where multiple semantic features are embedded into shared subspaces or overlapping neuron activations [29].

MONOSEMANTIC REPRESENTATIONS: A representation is called monosemantic when each neuron corresponds to a single interpretable feature [8]. Mathematically, this corresponds to the case where W is full-rank and aligned with the identity matrix (or a rotation of it):

$$W = I \Rightarrow \mathbf{h} = \mathbf{a}.$$

This implies that each feature a_i is represented by a unique dimension h_i , with no overlap. Each neuron responds to a single, isolated concept, akin to “grandmother cells” in neuroscience [37].

POLYSEMANIC REPRESENTATIONS: In contrast, polysemantic neurons represent multiple, distinct concepts. Formally, if neuron h_j computes:

$$h_j = \sum_{i=1}^F W_{j,i} a_i,$$

and two or more $W_{j,i} \neq 0$, then neuron j encodes multiple features simultaneously, exhibiting polysemanicity [29, 30].

More generally, a polysemantic embedding may be viewed as a mixture:

$$\mathbf{h} = \sum_{k=1}^K \alpha_k \mathbf{c}_k, \quad K > 1,$$

where \mathbf{c}_k are concept vectors and α_k are scalar weights.

This behavior is prevalent in both neural network activations and in biological neurons that exhibit mixed selectivity [38].

Monosemantic representations arise from disentangled bases, where neurons correspond to isolated features. Superposition emerges from dimensionality compression and necessarily leads to polysemantic neurons, each encoding a combination of features. Spare auto-encoder is a way to try to solve the polysemantic neurons—each encoding problem.

A.6 The SAE approach and architectures

Sparse Autoencoder (SAE) architectures have advanced our understanding of how language and vision models represent features [16]. Neural network behavior is often explained via *computational circuits*—collections of neurons that together compute meaningful functions. Classical circuit analysis has identified key components such as edge detectors [39] or word-copying units [30]. By using features derived from SAEs rather than raw neurons, researchers have improved the interpretability of circuits related to complex behaviors [40].

Feature discovery can involve visual analysis [41], manual inspection [42], and even assistance from large language models [43]. Their causal role is often validated via activation interventions: modifying a feature activation vector \mathbf{a} and observing predictable changes in model output [44].

The mathematical formulation situates SAE architectures within the theoretical framework of superposition and semantic disentanglement. By expressing hidden states as sparse linear combinations of interpretable features, SAEs bridge the gap between low-level activations and human-understandable concepts.

LINEAR FORMULATION OF SAEs: Let $\mathbf{x} \in \mathbb{R}^d$ denote a layer's neuron activation vector in a pretrained model. A Sparse Autoencoder learns a sparse feature representation $\mathbf{a} \in \mathbb{R}^F$ such that:

$$\hat{\mathbf{x}} = W\mathbf{a} + \mathbf{b}, \quad (40)$$

where $W \in \mathbb{R}^{d \times F}$ is the decoder (dictionary) matrix and $\mathbf{b} \in \mathbb{R}^d$ is a learned bias term. Each column $W_{:,i}$ represents the direction of feature i in neuron space, and a_i is its activation. This linear mapping enables complex activations to be expressed as combinations of more interpretable features.

If $F > d$, then the feature space is overcomplete, and W cannot be full-rank. This leads to superposition, where multiple features overlap in the same subspace, and individual neurons encode multiple unrelated concepts [29]. If W is invertible and aligned to a basis, each neuron corresponds to a single feature. The representation is monosemantic and disentangled [8]. When W has overlapping columns, neurons can respond to multiple features, yielding polysemantic behavior. That is, for some j , $x_j = \sum_i W_{j,i} a_i$ involves multiple nonzero terms [30].

VARIANTS OF SAEs: Variants of SAEs like TopK, JumpReLU, and Gated-SAEs offer increasingly precise control over the mapping between low-level activations and human-understandable concepts, enabling fine-grained analysis and intervention.

TopK-SAEs: Instead of using a soft sparsity constraint (e.g., L1 regularization), TopK-SAEs enforce hard sparsity using a top- K activation function:

$$\mathbf{a} = \text{TopK}(W_{\text{enc}}(\mathbf{x} - \mathbf{b}_{\text{dec}})), \quad (41)$$

which retains only the K largest entries of the preactivation and zeros out the rest. This promotes discrete sparsity and avoids complex hyperparameter tuning.

JumpReLU-SAEs: JumpReLU replaces ReLU with a thresholded step function:

$$\text{JumpReLU}_{\theta}(x) = x \cdot H(x - \theta), \quad (42)$$

where $H(\cdot)$ is the Heaviside step function and θ is a learnable threshold. This allows neurons to activate only above a semantic threshold, aligning with binary behavior observed in some interpretable features. However, the discontinuity makes training difficult due to non-differentiability.

Gated-SAEs: Gated-SAEs introduce a gating mechanism that decouples activation magnitude and presence. Let W_{mag} and W_{gate} be two encoders. Then the feature activation is computed as:

$$\mathbf{a} = (W_{\text{mag}}(\mathbf{x})) \odot H(W_{\text{gate}}(\mathbf{x}) - \theta), \quad (43)$$

where \odot denotes elementwise multiplication. This enables better control over when and how strongly a feature activates, making them easier to train than JumpReLU-SAEs [45].

In this study we utilize two different architectures of SAEs the standard SAE and TopK-SAE.

A.7 Attribution from Sparse Feature Space to Input Tokens

Let $\mathbf{x}_{\text{input}} \in \mathbb{R}^{d_{\text{input}}}$ denote the input embedding vector (e.g., LLM token embeddings), $\mathbf{x} = f(\mathbf{x}_{\text{input}}) \in \mathbb{R}^d$ the hidden layer activation of the LLM, $\mathbf{a} = \text{Encoder}(\mathbf{x}) \in \mathbb{R}^F$ the SAE sparse feature vector, and $\hat{\mathbf{x}} = W\mathbf{a} + \mathbf{b}$ the reconstructed activation from the SAE decoder. Now suppose we have a sparse attribution vector ψ_i over features \mathbf{a} , i.e., $\psi \in \mathbb{R}^F$,

where each ψ_i reflects the importance of SAE feature a_i . We aim to assign importance Φ_k to each input token dimension $x_{\text{input},k}$.

ATTRIBUTION FLOW THROUGH THE ENCODER: We propagate the feature attributions backward through the encoder to the input. Using the chain rule:

$$\Phi_k = \sum_{i=1}^F \psi_i \cdot \frac{\partial a_i}{\partial x_{\text{input},k}} = \sum_{i=1}^F \psi_i \cdot \frac{\partial a_i}{\partial \mathbf{x}} \cdot \frac{\partial \mathbf{x}}{\partial x_{\text{input},k}} \quad (44)$$

where $\frac{\partial a_i}{\partial \mathbf{x}}$ is the encoder Jacobian (SAE layer), and $\frac{\partial \mathbf{x}}{\partial x_{\text{input},k}}$ is the LLM gradient from input token to hidden layer.

This gives us a scalar attribution $\Phi_k \in \mathbb{R}$ for each token/input embedding dimension k .

This represents how much each input token contributes to the sparse SAE features that have been identified as important. In this way, we evaluate the contribution of input features based on the monosemantic behavior of the trained network's mechanism. Based on our study thus far, we will apply the six attribution methods previously discussed at two levels: from the SAE feature space to the encoder layer, and from the encoder layer to the input embedding space. This dual-level attribution analysis enables us to investigate how interpretable sparse features relate to model internals and ultimately influence the input-level representations.

To this end, we define a two-step attribution mechanism:

Step 1: Attribution from Sparse Features to Encoder Layer

Let $\psi \in \mathbb{R}^F$ represent the importance scores of sparse features (obtained via attribution methods). We propagate these to the encoder layer as:

$$\phi^{\text{enc}} = W\psi \in \mathbb{R}^d, \quad (45)$$

where ϕ^{enc} quantifies the contribution of each encoder neuron to the important SAE features.

Step 2: Attribution from Encoder Layer to Input

To assign attribution scores to input dimensions, we propagate ϕ^{enc} to the input embedding via the gradient of the encoder:

$$\phi^{\text{input}} = \left(\frac{\partial \mathbf{x}}{\partial \mathbf{x}_{\text{input}}} \right)^{\top} \phi^{\text{enc}} \in \mathbb{R}^{d_{\text{input}}}. \quad (46)$$

Alternatively, attribution methods (e.g., Integrated Gradients, SHAP) can directly estimate:

$$\phi^{\text{input}} = \text{AttributionMethod}(f, \mathbf{x}_{\text{input}}, \phi^{\text{enc}})$$

This dual-level attribution analysis allows us to connect semantically meaningful sparse features to the raw input representation space.

B Clinical Validation and External Interpretability Analysis

B.1 Clinical relevance in Alzheimer's diagnosis progression: Evidence that SAE-guided attribution yields more reliable explanations than traditional attribution.

To further validate the role of the SAE layer in shaping the attribution space into a more monosemantic and clinically coherent feature representation, we conducted an auxiliary evaluation. Specifically, for each test input, we extracted the top 50% most influential token attributions produced by our attribution framework—TEO without SAE, TEO with SAE, and TEO-UMAP. We then generated a CSV file for each classification class, in which the highlighted characters for the three attribution methods were organized column-wise. The complete character sequence for each sample, beginning with the CLS token, was included in the first column to ensure clear sample-level distinction. These CSV

files were subsequently provided as input to a large language model (ChatGPT-5.1 [35]) using a fixed prompt to obtain an external, model-agnostic assessment of the interpretability structure encoded by each explanation space. Three experiments were performed:

1. **Binary ADNI** (Control vs. Alzheimer's disease), with each class provided as a separate CSV file.
2. **Binary BrainLAT** (Control vs. Alzheimer's disease), also split into two class-specific CSV files.
3. **Three-class ADNI** (Control, MCI, LMCI), with each diagnostic category represented in its own CSV file.

We evaluated two primary criteria: (i) whether the language model could distinguish, based solely on the highlighted features, which CSV corresponded to the pathological versus the healthy control class; and (ii) whether the model could identify meaningful pathology-related biomarkers.

For the first two experiments, the model was prompted with:

Given the two CSV files, and recognizing that medical biases exist in the char column with each sample beginning with the character sequence [CLS], determine how each of the three attribution methods (attr1, attr2, attr3) highlight features associated with healthy or unhealthy interpretations, and analyze the reasons for these differences. Predict the pathology and specify which of the two CSV files corresponds to the pathological case for each attribution technique.

For the three-class ADNI experiment, we used:

Given the three CSV files, and recognizing that medical biases exist in the char column with each sample beginning with the character sequence [CLS], determine how each attribution method (attr1, attr2, attr3) highlights features associated with healthy or pathological interpretations. Predict the pathology or pathologies, identify which CSVs correspond to the pathological and healthy groups for each attribution method, and specify the associated conditions.

The resulting GPT-generated interpretations, shown in Figures 4, provide an external linguistic lens on each explanation space.

In the binary ADNI experiment, all the three attribution frameworks, TEO without SAE, TEO with SAE, and TEO-UMAP, correctly identified the pathological file (CSV1) and associated it with Alzheimer's disease, noting that the signal was more consistent with late-stage rather than early cognitive impairment. A similar pattern emerged for the binary BrainLAT experiment: the pathological CSV was attributed to Alzheimer's disease rather than MCI, with clear differentiation from the healthy control (Figures 4a,b).

Across both binary tasks, TEO without SAE exhibited erratic and clinically uninformative behavior, frequently attending to task labels, instruction counts, or other artefactual patterns rather than neurocognitive biomarkers (Figures 4a,b). In contrast, TEO-SAE and TEO-UMAP consistently highlighted clinically meaningful domains, including demographic risk factors, processing-speed impairments, and neurophysiological indicators.

In the more complex three-class ADNI experiment, the advantages of the SAE-induced monosemantic structure became even clearer (Figure 4c). TEO without SAE failed to correctly identify pathological classes and did not surface meaningful biomarkers. Conversely, TEO-SAE achieved clearer diagnostic separation and more coherent feature concentrations, while TEO-UMAP further emphasized structured biomarkers, particularly within demographics and vitals, and also provided correct class-level predictions.

Collectively, these findings demonstrate that incorporating the SAE layer—thereby enforcing a more monosemantic, disentangled attribution representation—substantially enhances the clinical meaningfulness, stability, and diagnostic alignment of the resulting explanations.

B.2 The clinical impact and outcome in the diagnosis of Alzheimer, early MCI and late MCI.

This study shows that the Transformer Explanation Optimizer (TEO) with a Sparse Autoencoder (SAE) and TEO-UMAP provide the most reliable identification of informative sources across nine multimodal subgroups: Demographics (DEM), Vital Signs (VS), Clock Drawing Test (CDT), Clock Copying Test (CCT), Auditory Verbal Learning Test v1 (AVLT1), Category Fluency—Animals (CFA), Auditory Verbal Learning Test v2 (AVLT2), American National Adult Reading Test (ANART), and Functional Activities Questionnaire (FAQ). Using a significance threshold of 0.6 on PCA principal components PC1, we observe in the binary task that, for Control, TEO-SAE is dominated by FAQ, whereas TEO-UMAP emphasises DEM, AVLT2, and FAQ; for Alzheimer's, TEO prioritises FAQ, AVLT1, and CFA, while TEO-UMAP highlights ANART, FAQ, and DEM. In the three-class task, for Control the main contributors are

Table 2: Relative contribution of multimodal assessment groups across diagnostic categories and attribution methods.

Group	Dem	VS	CDT	CCT	AVLT1	CFA	AVLT2	ANART	FAQ
<i>Binary classification (Control vs. Alzheimer's disease)</i>									
Control (TEO)	0.00	0.00	0.00	0.00	0.02	0.00	0.00	0.00	0.11
Control (TEO-UMAP)	0.33	0.21	0.29	0.29	0.12	0.30	0.32	0.30	0.36
Alzheimer (TEO)	0.05	0.00	0.09	0.01	0.12	0.12	0.00	0.00	0.13
Alzheimer (TEO-UMAP)	0.33	0.29	0.30	0.32	0.22	0.30	0.32	0.50	0.35
<i>Three-class classification (Control / MCI / LMCI)</i>									
Control (TEO)	0.74	0.55	0.87	0.63	0.88	0.68	0.20	0.80	0.38
Control (TEO-UMAP)	0.51	0.61	0.67	0.60	0.72	0.66	0.56	0.60	0.45
MCI (TEO)	0.23	0.30	0.29	0.38	0.22	0.30	0.36	0.10	0.31
MCI (TEO-UMAP)	0.31	0.26	0.21	0.22	0.22	0.36	0.40	0.40	0.23
LMCI (TEO)	0.19	0.19	0.20	0.10	0.22	0.16	0.24	0.10	0.22
LMCI (TEO-UMAP)	0.32	0.27	0.23	0.25	0.24	0.28	0.40	0.40	0.43

Abbreviations: Dem = Demographics; VS = Vital Signs; CDT = Clock Drawing Test; CCT = Clock Copying Test; AVLT1/2 = Auditory Verbal Learning Test (v1/v2); CFA = Category Fluency (Animals); ANART = American National Adult Reading Test; FAQ = Functional Activities Questionnaire.

AVLT1, CDT, and ANART under TEO, and AVLT1, CDT, and CFA under TEO-UMAP; for MCI, TEO favours CCT, AVLT2, and FAQ, whereas TEO-UMAP favours AVLT2, ANART, and CFA; and for LMCI, TEO elevates AVLT1, FAQ, and CDT, while TEO-UMAP elevates FAQ, ANART, and AVLT2. These patterns, summarised in Table 2, support the clinical interpretability of the proposed optimisers.

Across ADNI cohorts, the most stable signals for clinical stratification are functional status (FAQ) and memory measures (AVLT1/AVLT2), with visuospatial performance (CDT) recurrent in Control/LMCI. TEO+SAE preferentially elevates neuropsychological performance features (AVLT1/2, CDT, CCT), while TEO-UMAP surfaces complementary contextual and language markers (DEM, ANART, CFA), yielding class-specific, interpretable profiles: Control—FAQ/AVLT1/CDT; Alzheimer’s—FAQ with AVLT1/CFA (TEO) or ANART/DEM (TEO-UMAP); MCI—AVLT2 with CCT/FAQ (TEO) or ANART/CFA (TEO-UMAP); and LMCI—FAQ with AVLT1/CDT (TEO) or ANART/AVLT2 (TEO-UMAP). Using a simple $PC1 \geq 0.6$ significance rule, these optimisers provide actionable attribution maps that can prioritise assessments, reduce testing burden, support trial enrichment, and guide personalised monitoring. Together, they offer a practically deployable and transparent framework for clinically meaningful multimodal reasoning in neurodegenerative disease.

B.3 Validation of the UMAP Linear Constraint via PCA Structure Analysis

To verify the claim that the proposed UMAP linear constraint effectively linearizes the majority of the attribution space and yields robust attribution scores within the same tokenized feature, we performed an additional PCA analysis. Specifically, we extracted the top eight principal components from the attribution matrix and visualized the first two components, which capture the highest proportion of variance in the data. This allows us to assess whether the tokenized features exhibit an approximately linear structure in their dominant statistical directions. The results (Figure 2) demonstrate that the proposed method indeed produces an embedding that approaches a linear configuration, thereby supporting our hypothesis that the UMAP linear constraint leads to more stable and structurally consistent attribution representations.

B.4 Related Work

B.4.1 Attributional Interpretability

Attributional interpretability (AtI), a branch of explainable AI (XAI), focuses on explaining model outputs by tracing predictions back to individual input contributions, often using gradient-based methods [46]. While gradients provide insights into the relationship between inputs and outputs, they can be sensitive to perturbations or discontinuities, posing challenges for reliable interpretation.

AtI encompasses various methods for interpreting complex, nonlinear models, including techniques like Local Interpretable Model-agnostic Explanations (LIME; [47]) and SHapley Additive exPlanations (SHAP; [23]). In medical

imaging, popular attribution techniques include SHAP, Layer-wise Relevance Propagation (LRP; [48]), and gradient-based methods like GRAD-CAM ([49]). These methods aim to enhance trust in models and provide valuable insights into decision-making processes. However, they face limitations. For instance, LRP emphasizes positive preactivations, often yielding less precise explanations, while SHAP is computationally intensive due to the complexity of calculating Shapley values [23]. Adaptations like Monte Carlo methods and stratified sampling (e.g., SVARM) have improved the efficiency and precision of certain techniques [50].

B.4.2 Mechanistic Interpretability and Sparse Autoencoder

Mechanistic interpretability (MI), a key area of explainable AI (XAI), focuses on understanding the internal activation patterns of AI models by analyzing their fundamental components, such as features, neurons, layers, and connections. Unlike AAI, MI takes a bottom-up approach, aiming to uncover the causal relationships and precise computations that transform inputs into outputs. This method identifies specific neural circuits driving behavior and provides a reverse-engineering perspective. Insights from fields like physics, neuroscience, and systems biology further guide the development of transparent and value-aligned AI systems.

A core principle of MI is the concept of polysemanticity, where individual neurons encode multiple concepts, contrasted with monosemanticity, where neurons correspond to a single semantic concept. Polysemanticity reduces interpretability, as neurons represent overlapping features. Structures like sparse autoencoders (SAEs) address this by leveraging the superposition hypothesis, which posits that neural networks use high-dimensional spaces to represent more features than the number of neurons, encoding them in nearly orthogonal directions. SAEs decompose embeddings from deep layers, such as MLPs or transformer attention layers, into higher-dimensional monosemantic representations, aligning activation patterns with specific concepts of interest [9, 51].

Sparse Autoencoder architectures have significantly advanced our understanding of feature representations in language and vision models [16]. Neural network behavior is often interpreted through *computational circuits*—groups of neurons that compute meaningful functions, such as edge detectors [39] or word-copying units [52]. Leveraging SAE-derived features instead of raw neurons has improved the interpretability of circuits associated with complex behaviors [40]. This shift enables clearer mappings between neuron activations and high-level functions, facilitating validation of model behavior [46]. By aligning internal representations with privileged basis directions—distinct semantic vectors within network layers—researchers further enhance monosemanticity and advance the interpretability of deep models.

Two-class ADNI classification experiment

Binary ADNI Control (0)**Binary ADNI Alzheimer (1)**

Given the two CSV files, and recognizing that medical biases exist in the char column with each of samples beginning with the character sequence [C L S], determine how each of the three attribution methods (attr1, attr2, attr3) highlights features that may be associated with healthy or unhealthy interpretations, and analyze the reasons for these differences. Try to predict the pathology. Mention which of the two csv files highlight the pathological case for each of the three attr techniques and try to specify the pathology.

Method	What It Highlights Most	Which CSV Shows the Pathological Pattern	Why This CSV Looks Pathological	Likely Pathology Suggested
attr1	Score terms (Total, Intrusions, Correct), demographic fields (Birth year, education, Race), test-related error wording	CSV 1	Stronger emphasis on demographic risk indicators and on error-related cognitive test features	Amnestic cognitive disorder (likely early Alzheimer's / amnestic MCI)
attr2	Task names, specific scores, intrusion counts, slow Trails B areas	CSV 1	More attention to the worst-performing cognitive segments and to demographic correlates	Amnestic cognitive disorder (likely early Alzheimer's / amnestic MCI)
attr3	Whole neuropsych blocks (Clock, AVLT, Trails), demographic segments, sections with intrusions or slow processing	CSV 1	Highlights both demographic risk factors and impaired memory/executive performance more strongly	Amnestic cognitive disorder (likely early Alzheimer's / amnestic MCI)

Two-class BrainLAT classification experiment

Binary BrainLAT Control (BL_0)**Binary BrainLAT Alzheimer (BL_1)**

Given the two CSV files, and recognizing that medical biases exist in the char column with each of samples beginning with the character sequence [C L S], determine how each of the three attribution methods (attr1, attr2, attr3) highlights features that may be associated with healthy or unhealthy interpretations, and analyze the reasons for these differences. Try to predict the pathology. Mention which of the two csv files highlight the pathological case for each of the three attr techniques and try to specify the pathology.

Method	What It Highlights Most	Pathological CSV	Why This CSV Appears Pathological	Suggested Pathology
attr1	Notable emphasis on key cognitive-test terms, scoring markers, and error-related text segments	BL_1	Shows greater sensitivity to segments containing performance weakness indicators and demographic risk markers	Memory-dominant cognitive deficit (amnestic MCI / early Alzheimer's)
attr2	Focus on specific task labels and parts of the text associated with reduced performance or irregular responses	BL_1	Highlights sections where performance is most impaired, such as memory intrusions or slowed sequences	Amnestic pattern consistent with early neurodegenerative disease
attr3	Broad blocks of neuropsych content, especially where errors, slow timing, or intrusions appear	BL_1	Shows widespread emphasis across impaired-performance regions and demographic variables	Early Alzheimer's-type cognitive impairment

Figure 4: GPT-5.1 generated global explanations characterizing attribution-score performance in biomarker identification for TEO, both with and without the SAE layer, and for the TEO-UMAP model. (a) Binary ADNI: Control vs. Alzheimer's disease. (b) Binary BrainLAT: Control vs. Alzheimer's disease.

Three-class ADNI classification experiment

Three class ADNI Control (0) Three class ADNI MCI (1) Three class ADNI LMCI (2)

Given the three CSV files, and recognizing that medical biases exist in the char column with each of samples beginning with the character sequence [C L S], determine how each of the three attribution methods (attr1, attr2, attr3) highlights features that may be associated with healthy or unhealthy interpretations, and analyze the reasons for these differences. Try to predict the pathology or pathologies and the healthy if exist. Mention which of the three csv files highlight the pathological case/s for each of the three attr techniques and try to specify the pathology/ies and the same for the healthy (control if exist).

Attribution Pattern Type	Behavior Observed in CSV File 0	Behavior Observed in CSV File 1	Behavior Observed in CSV File 2	Interpretation (Pathology / Healthy)
Pattern Type A (very sparse, near-zero emphasis overall)	Minimal highlighting of any medically relevant fields; almost all characters left unmarked.	Slight but still very limited emphasis on demographic fields and test labels.	Noticeably more highlighting on demographics, test headers, and structural elements of the note compared to CSV 0 and 1.	CSV 0 corresponds best to healthy / control class . CSV 1 corresponds to milder pathology , CSV 2 to more severe pathology .
Pattern Type B (extremely flat, low-information pattern)	Very low number of highlighted characters; almost uniformly neutral.	Similarly low highlighting; no meaningful differentiation.	Same low-density pattern; virtually no medically decisive areas marked.	This pattern does not meaningfully distinguish healthy vs pathological classes across any CSV files.
Pattern Type C (dense, diffuse, broad coverage)	Broad but slightly lower coverage of demographic fields, vitals, and test labels.	Broad coverage similar to CSV 2 but with slightly less emphasis.	Highest density: demographics, vitals, and test labels consistently highlighted.	CSV 0 again aligns with healthy / control . CSV 1 and CSV 2 align with pathology classes , with CSV 2 indicating more severe pathology .

Figure 5: (continued) (c) Three-class ADNI: Control, MCI, and LMCI categories.